UC Santa Barbara

UC Santa Barbara Electronic Theses and Dissertations

Title

Central Asia’s hydroclimate response to Heinrich events 4 and 5

Permalink

https://escholarship.org/uc/item/2fm033xk

Author

Berberian, Lori Aznive

Publication Date

2022

Peer reviewed|Thesis/dissertation

eScholarship.org Powered by the California Digital Library
University of California

UNIVERSITY OF CALIFORNIA

Santa Barbara

Central Asia's hydroclimate response to Heinrich events 4 and 5

A Thesis submitted in partial satisfaction of the

requirements for the degree Master of Science in Earth Science

by

Lori Aznive Berberian

Committee in charge:

Professor Syee Weldeab, Chair

Professor Lorraine Lisiecki

Professor Morgan Raven

June 2022

The thesis of Lori Aznive Berberian is approved.

_____

Lorraine Lisiecki

_____

Morgan Raven

_____

Syee Weldeab, Committee Chair

June 2022

Central Asia's hydroclimate response to Heinrich events 4 and 5

Copyright © 2022

By

Lori Aznive Berberian

DEDICATION

This thesis is dedicated to my cousin Luke R. Laufenberg,

whose wisdom always guides me through life's challenges.

ACKNOWLEDGEMENTS

I would like to thank Dr. Anderw Kylander-Clark of the UCSB Cloud Lab for the trace element analysis; UCSC's Stable Isotope Lab for the analysis of carbon and oxygen isotope data; and Professors Lorraine Lisiecki, Morgan Raven, and Syee Weldeab (the academic thesis committee) for their review of this thesis. Professor Weldeab and I would like to thank Professor David McGee at MIT for carrying out the U-Th age dating of the stalagmite. Sampling, sample preparation and analyses of U-Th data were carried out prior to my arrival at UCSB. U-Th data were provided to me by my thesis advisor, Syee Weldeab, for completion of my Master's research and this thesis.

I would also like to thank my peers, Bets Hobart, Devin Rand, and Elisa Emedri as well as, my family Sarkis, Rebecca, Alique, Nareg, Nazan, Nareg, Serop and Lavash for their support thorough my time at UCSB.

ABSTRACT

Central Asia's hydroclimate response to Heinrich events 4 and 5

By

Lori Aznive Berberian

Documentation of mid-latitude hydroclimate responses to late Pleistocene North Atlantic climate change is sparse and fragmented due to a lack of continuous and well dated reconstructions. Here we analyze the remote effects of Heinrich events to understand the relationship between periods of North Atlantic climate changes and Central Asia's precipitation variability. We analyzed trace element, $\delta^{18}O$ and $\delta^{13}C$ data as proxies for precipitation variability. Comparison of these proxies with climate records of northern hemisphere high and low latitude climate changes reveals several episodes of increased precipitation over Central Asia that coincide with cooling of the northern high latitude and weakening of northern hemisphere monsoon. We propose two atmospheric links between the North Atlantic and Central Asia which likely brought increased moisture to the region during Heinrich events 4 and 5: the Westerly Jet and Siberian High.

TABLE OF CONTENTS

LIST OF FIGURES

1. Introduction

Currently, accelerated melting of the Greenland ice sheet is contributing to the observed weakening of the Atlantic meridional overturning circulation (AMOC), a system of ocean currents in the North Atlantic redistributing global heat and thereby affecting Earth's climate (Caesar et al., 2018; Lenton et al., 2008; Rahmstorf, 2000). The impact of past instances of meltwater-induced AMOC weakening, known as Heinrich events, on atmospheric and oceanic circulation is relatively well documented, particularly in the high and low latitudes (Hemming, 2004; Barker et al., 2015; Knutti et al., 2004; Wang et al., 2001; Novello et al. 2017, Strikis et al. 2018, Ma et al., 2021; Kindler et al., 2014; Matrat et al., 2007; Weldeab et al., 2021). However, documentation of hydroclimate responses in the mid-latitudes is sparse and fragmented due to lack of continuous and well dated hydroclimate reconstructions. Here we analyze the effects of North Atlantic climate change on Central Asia's precipitation variability during millennial-scale episodes of meltwater input in the North Atlantic Ocean.

Studying the response of Central Asia's precipitation to previous episodes of AMOC weakening may help us understand the general mechanisms potentially linking North Atlantic climate with Central Asia's hydroclimate. Using geochemical multi-proxy data from stalagmites, we present a hydroclimate reconstruction of Central Asia (34-50 kyr BP). The results of this study reveal Central Asia's hydroclimate variability coincident with the timing of Heinrich events 4 and 5 that occurred at 38-40 and 47-49 kyr BP, respectively (Kindler et al., 2014; Knutti et al., 2004; Rasmussen et al., 2003). Located far from immediate influence of global oceans, evidence for regional precipitation changes during this time window implies atmosphere teleconnections between Central Asia and the North Atlantic.

Understanding the response to past meltwater-induced AMOC weakening on regional continental climates such as Central Asia, will provide insight on hydroclimate variability in midlatitude semi-arid winter rainfall zones. Precipitation reconstruction from Central Asia could inform models for evapo-transportation and water source during North Atlantic climate perturbations. This work may therefore improve models of Central Asia's response to ongoing global warming and ice-sheet melting. Central Asia is more vulnerable to the consequences of climate change than most other regions of the world (IPCC, 2014). According to recent climate simulations (Hijioka et al., 2014) Central Asia is expected to become warmer in the coming decades and increasingly arid, especially in the western region encompassing southwest Kyrgyzstan. The results from this study may help improve our general understanding of Central Asia's climate response to global climate changes.

1.1 Background

Heinrich events are recorded in North Atlantic Ocean sediment as layers with high concentrations of ice-rafted debris (IRD) delivered by melting icebergs (Heinrich 1988; Hemming et al., 2004). The fresh water input from melting icebergs decreases the density of the North Atlantic surface waters and as a result, weakens the formation of North Atlantic deep water (Rahmstorf, 2006). In turn, this slows down the AMOC reducing heat transport to the North Atlantic Ocean and consequently cooling the sea surface temperature (SST). Conversely, in the southern-mid and high latitudes, heat builds up in the Southern Ocean warming the southern hemisphere (Knutti et al., 2004).

Recent climate model assessments have demonstrated ocean-atmosphere coupling during periods of abrupt cooling in the North Atlantic region at seasonal-millennial time scales (e.g., Gastineau et al., 2015; Gastineau et al., 2013). The effects of the North Atlantic cooling and attendant changes in atmospheric circulation is well documented in weakening and strengthening of northern and southern hemisphere monsoon systems (Strikis et al., 2018; Cruz et al., 2005; Wang et al., 2001; Weldeab et al., 2007; Ma et al., 2021). However, the midlatitude climate zone is under sampled. As a result, our understanding of its climate response to global climate changes including North Atlantic cooling, is fragmentary.

The mechanisms initiating Heinrich events are debated as at least three different hypotheses have been put forward. MacAyeal (1993) proposed that ice rafting events originated from instability and collapse of the Laurentide ice sheet in eastern Canada. Bond et al. (1993) presented a hypothesis where Heinrich events were triggered by Dansgaard-Oeschger (D-O) oscillations. D-O oscillations are transitions from warm interstadial and cold stadial conditions preceding Heinrich events. According to Bond et al. (1993), during D-O interstadials sea level rise would have resulted in buttressing and undercutting of the Laurentide Glacier starting the Heinrich events. In contrast, Barker et al. (2015) argued Heinrich events were caused by gradual cooling across the North Atlantic and did not trigger abrupt transitions to stadial conditions. While this remains a matter of debate, the impact of Heinrich events on high latitude and tropical hydroclimates is well documented. Here we aim to improve our understanding of Central Asia's hydroclimate response to meltwater-induced perturbations of oceanic and atmospheric circulations.

2. Regional climate and cave site description

Central Asia encompasses Kazakhstan, Kyrgyzstan, Uzbekistan, Tajikistan and Turkmenistan. Located between semi-arid (<10 cm precipitation/year) and desert (< 25 cm/year) climate zones, western Central Asia–the driest region with a desert climate–is surrounded by semiarid areas on the norther, eastern and southern ends. Central Asia's climate is largely influenced by its topography, strength of the Westerly Jet stream and associated moisture fluxes (Schiemann et al., 2008). Due to the extreme topographic relief of the region (90 m below sea level near the Caspian Sea and > 7,000 m along the Himalayas), there are large gradients in annual rainfall, varying between < 50 mm per year in desert areas and 900 mm in the mountains (de Berus et al., 2018; Bothe et al., 2012). Most of Central Asia's precipitation falls as snow during the cold season (November–March) (Gerlitz et al., 2018) at the southern edge of the Tibetan Plateau along the Himalayan mountains and is released as snowmelt in the summer (Figure 1a–1b).

The region's moisture fluxes are modulated by several climate modes. Previous studies (e.g., Gerlitz et al., 2018; de Beurs et al., 2018) have linked global climate oscillations, such as the El Niño–Southern Oscillation (ENSO) and the North Atlantic Oscillation (NAO) to winter precipitation in the southern parts of Central Asia in the last 20 to 50 years. The El Niño phase causes the formation of anticyclones over the western Indian Ocean and an increase in tropical moisture fluxes, heat delivered to Central Asia. La Niña promotes an anticyclonic anomaly over central Asia, resulting in drier conditions. In combination with enhanced moisture supply during El Niño, wind patterns such as intensified mid-latitude Westerlies (moist westerly Atlantic air masses) further increase the moisture flux to this remote region.

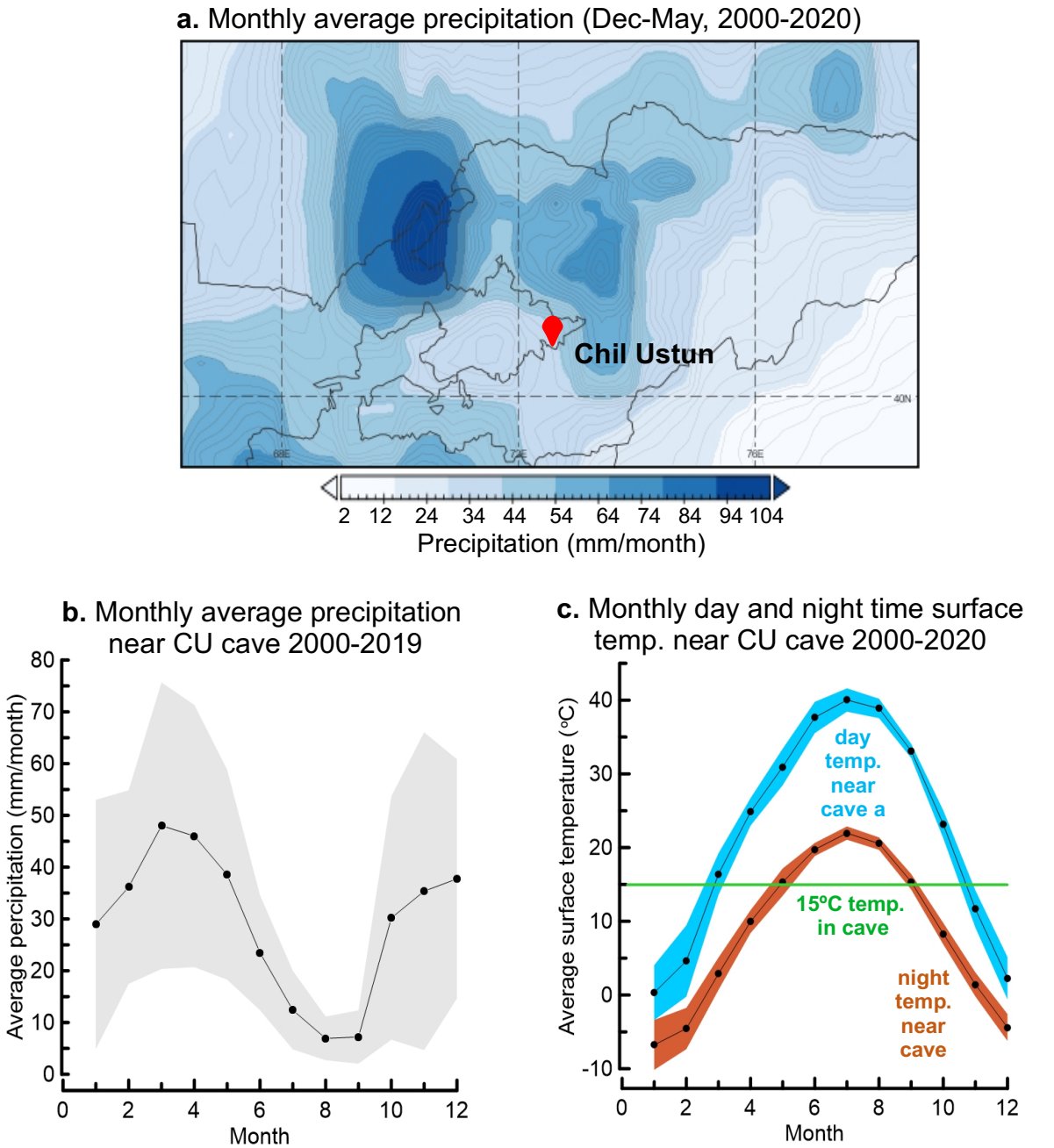

Figure 1. Study site, precipitation map and data: a. Monthly average precipitation between December and May (DJFMAM) 2000-2020. Chill Ustun (CU) cave is marked with red dot (72.53 E 40.52 N) (TRIM, 2011). b. Monthly average precipitation over CU cave 2000-2019, shows highest amounts of rainfall occurring in the first 6 month (DJFMAM) of each year from 2000-2019 (TRIM, 2011). Black line represents the monthly average precipitation in (mm/month), grey envelope shows the maximum and minimum values deviating from the average precipitation (mm/month). c. Monthly day and night time average surface temperature near CU cave 2000-2020 (Wan et al., 2015) The data show surface temperature (Cº) measured near CU cave during the day (blue: maximum and minimum average surface temperature) and night (orange: maximum and minimum average surface temperature). Green line represents constant cave temperature with an average (~15 ºC) (cave temperature data were provided by

Weldeab for only for the purpose of this thesis). Data shows a decrease in night time temperature by ~ 20ºC from day time max surface temperature to night time max surface temperate. With the exception of temperature data measured inside the cave, all data shown in Figure 1a–c were accessed through and obtained from Giovanni online data system, developed and maintained by the NASA GES DISC.

The stalagmite (CU1-1) used in this study was collected from Chil-Ustun (CU) Cave (72.53 E, 40.52 N, 1026 m above sea level), which is located in southwestern Kyrgyzstan (Figure 1a). The cave consists of several chambers that are interconnected by narrow passages. CU1-1 was collected from the last chamber, 800-900 m from the cave entrance and ~80 m below the surface. Hourly ambient temperature measurements were taken outside the cave over a period of 10 months (June 22, 2014 and April 28, 2015). Over the observed period daily air temperature outside the cave varied seasonally between 20˚C and 40˚C. Hourly ambient temperature measurements were taken inside the cave over a period of 11 months (June 22, 2014–June 8, 2015), which showed an average temperature of 14.86 ± 0.03˚C (n=7920). The monthly average surface air temperature outside the cave from 2000 and 2020 was 5.24 ± 2.7˚C in the Winter, 9.39 ± 1.9˚C in the Spring, 20.75 ± 0.9˚C in the Summer, and 8.37 ± 1.4˚C in the Fall (Figure 1c).

The cave is covered by many meters of limestone and massive host rock. Given its uniform composition, we can estimate the time for the cave environment to change as a function of depth and limestone diffusivity, assuming only diffusive heat conduction. The penetration length, defined by $x_{step} = \sqrt{2at}$ (Badino, 2004) approximates the time (t) it would take to change the temp inside the cave for a specified depth (x) and rate of limestone thermal diffusivity ($a=1.0\times10^{-6}$ m^2 s^{-1}; Lide, 2020). The thickness of the limestone roof where our sample was collected is ~80 m. We can therefore assume that changes in temperature would

be reflected in the cave during abrupt changes in outside surface temperature for an extended duration (~50 yrs). Based on our calculations, temperatures within the cave remained relatively constant during the Holocene and may have varied during glacial and interglacial periods.

3. Materials and methods

The stalagmite was embedded in resin, cut into three slabs with a circular saw on either end of the growth axis and washed in deionized water. The center slab was then cut into segments and polished with polishing material to obtain a smooth surface for various analysis. The segment CU1-1, discussed in this paper, consist of the upper 5.45 cm of the larger stalagmite segment.

3.1 U-Th dating:

Uranium-Thorium dating on the stalagmite segment was carried out in the laboratory of Professor David McGee at MIT. The following methods for U-Th dating are as described by Marks et al., (2021). Using a vertical mill, dating samples were drilled into ~ 150 mg powders, dissolved and spiked with a ^{229}Th–^{223}U–^{236}U tracer. U and Th were isolated via coprecipitation with iron oxyhydroxides and removed by means of a solvent–concurrent with methods in Edwards et al. (1987). Each dating sample included a total procedural blank. Fractionations of U and Th were measured on a Nu Plasma II-ES MC-ICP-MS (Burns et al., 2016). Correction for initial ^{230}Th was calculated using an initial ^{230}Th/ ^{232}Th atomic ratio of $4.4 \pm 2.2 \times 10^{-6}$ (Taylor and McLennan, 1985). The age model of CU1-1 consists of 5 U-Th data points and the 2sigma dating uncertainty ranges from ±0.20 and ±0.37 kyr BP.

Table. 1 U-Th age dating results

Sample ID	sampling depth interval (mm)	average sampling depth (mm)	Age (kyr)	± (2σ) kyr
CU1-T	2.5-5	3.75	36.63	0.27
CU1-1a	9.0-10	9.5	39.66	0.23
CU1-1b	17.5-19	18.25	45.51	0.20
CU1-1c	24.5-25.5	25	46.99	0.37
CU1-1d	30.5-32	31.25	48.80	0.28

3.2 Trace element analysis:

Measurements of Mg, Sr, Ba, P, U, Ca, Na, Al and Si concentrations were carried out using a Laser Ablation Inductively Coupled Plasma Mass Spectrometer (LAICP-MS) (Figure 2a) at the Department of Earth Science, UCSB. Using the Analyte 193 ArF laser-ablation system, measurements were collected from a 5.45 cm line along the growth axis of the cut and polished stalagmite segment (CU1-1) (Figure 2b) in a continuous sampling path with a $\pm$ 2µm uncertainty to the left or right. The Analyte 193 is based on an ATLEX SI ArF 193 nm wavelength excimer laser and equipped with a low-volume HeLex sample cell modified from the design of Eggins et al. (1998, 2005) (Kylander et al., 2013). The laser aerosol is carried by He from the sample cell to a mixing bulb in which the sample + He is mixed with Ar to stabilize the aerosol input to the plasma. Using boiled liquid argon and high-purity He the sample passes through activated charcoal and gold-coated quartz filters. The He–Ar aerosol is immediately split upon exiting the mixing bulb, with approximately half the ablation stream directed to each ICP-MS. Elemental abundances and their uncertainties are calculated by interleaving matrix-matched reference materials among samples and then reducing the collected data using the Iolite software (Woodhead et al., 2007; Paton et al., 2010).

The instrument is calibrated using synthetic silicate glasses NIST; Basalt, Hawaiian Volcano Observatory (BHVO) Hawaiian Island Basalt. A house standard, CU5–a nano-particulate pressed calcite powder tablet made from a stalagmite collected from the same cave (Prepared by Garbe-Schönberg and Weldeab, for method see Garbe-Schönberg and Müller, 2014)–was used to assess the reproducibility of the collected trace element data (Figure 3). In a split sample from the material used to make the tablet, wet chemistry analyses of elements were carried out using ICP-MS (Weldeab, personal communication–see Figure 3). House standard, CU5, data fall within the average values for wet chemistry analysis demonstrating reproducibility of the instrumentation measurements.

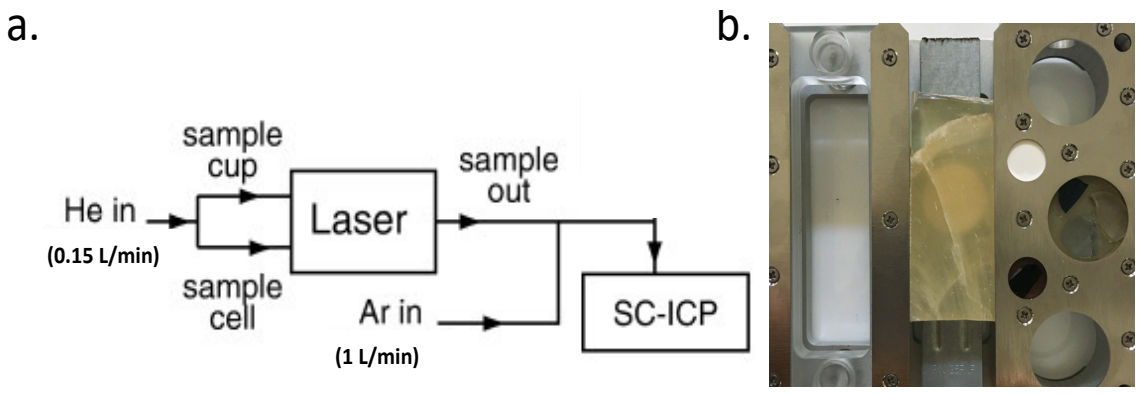

Figure 2. a. Instrumentation setup for laser-ablation-split stream (LASS) **b.** Polished CU1-1 segment (2 x 5.45 cm) in the LAICP sampling tray.

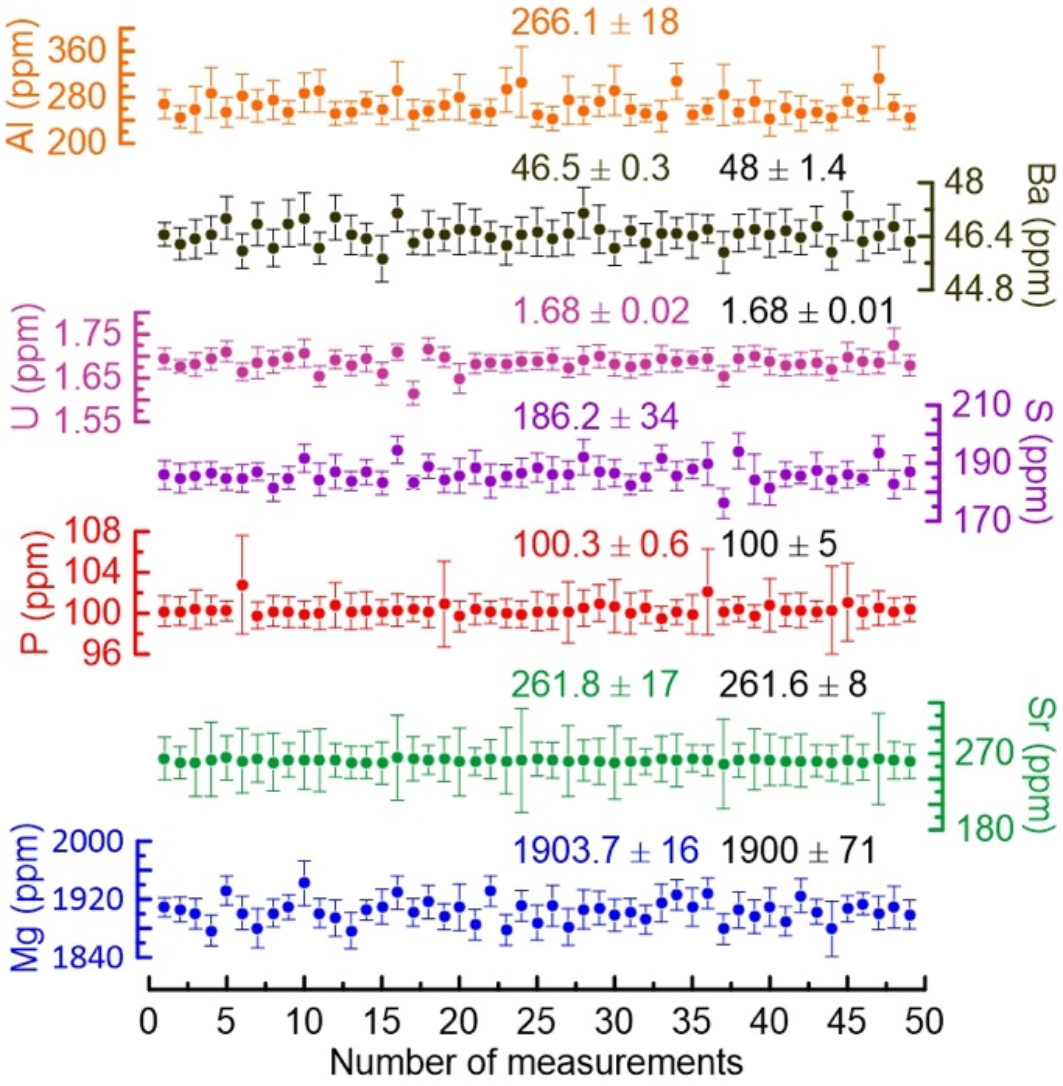

Figure 3. Repeat measurements of select elements in CU5 to check reproducibility during the trace element analysis of CU1-1. CU5 consists of nano-particulate pressed calcite powder tablet (prepared Garbe-Schönberg and Weldeab, for method see Garbe-Schönberg and Müller, 2014). Dots and vertical bars indicate the mean and deviation from the mean in a profile measurement of the CU5. Values in black indicate average values obtained using wet chemistry analysis (ICP-MS) of the powder that was used to create the pressed tablet (wet chemistry data provided by Weldeab for the purpose of this thesis).

3.3 Stable Isotope Analysis

CU1-1 was sampled at 100 µm intervals for $\delta^{18}O$ and $\delta^{13}C$ analysis with a sample size between 50 and 80 µg. Measurements were taken at the University of California, Santa Cruz using a Stable Isotope Ratio Mass Spectrometer (SIR-MS: MAT253) coupled to an online sample preparation device (Kiel IV). The errors associated with the analyses of $\delta^{18}O$ and $\delta^{13}C$ is ±0.70 and ±0.03 ‰, respectively

4. Results

4.1 U-Th Dating and Age model

Uranium concentration in CU1-1 is greater than 0.5 ppm and common Thorium (^{232}Th) is low ($2.3*10^{-4}$ –$2.9*10^{-3}$ ppm), resulting in relatively precise ^{230}Th age estimates (Table 1). The dating uncertainty (±2σ) varies between 0.20 and 0.37 kyr. All U-Th ages are in stratigraphic order. While the growth rate of CU1-1 varies significantly, there is no visual indication that the stalagmite contains growth gaps or hiatuses.

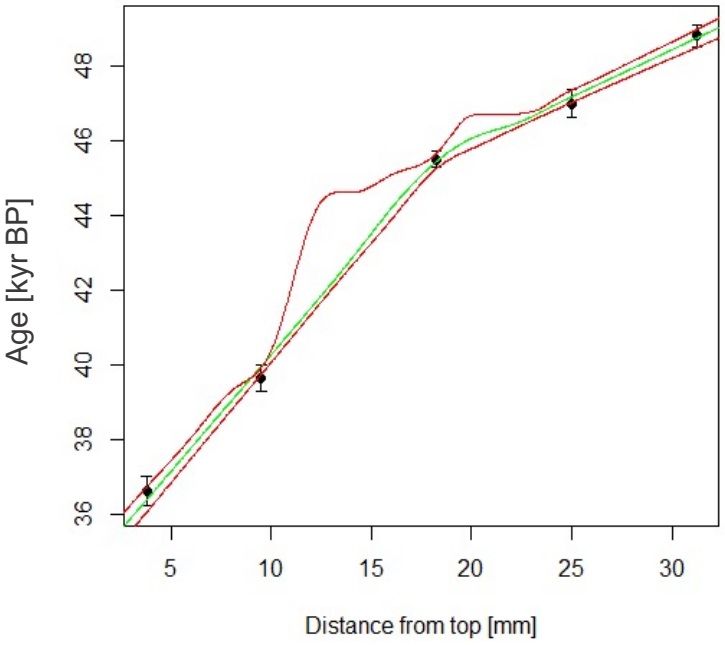

Figure 4. Age model: The red line represents the 95% confidence interval of the fitted model. The vertical black whiskers correspond to upper and lower U-Th age uncertainty (ranging from ±0.20 and ±0.37 kyr BP) (Table. 1) in CU1-1. The green line is the mean of the resampled subset. One subset consists of at least three adjacent points.

The CU1-1 age model (Figure 3) was developed using 5 Uranium-Thorium age control points (Table. 1) and age model software called "StalAge" (Scholz and Hoffmann, 2011). The age model's 95%-confidence envelope (red line, Figure 3) are calculated using a Monte-Carlo simulation (300 iterations) fitting ensembles of straight lines to sub-sets of the age data consisting of 3 adjacent points. The Monte-Carlo approach randomizes all dates within their uncertainty and for each iteration conducts a least-squares fit of a sequence of line segments for which growth rate must be positive but less than an arbitrary threshold (~1 mm/yr). The age model software has no adjustable free parameters. Potential outliers and age inversions are determined as follow: (1) if a straight line does not intersect the 2 sigma error bars of all points, or (2) if the slope of a possible straight line is negative. The final age model (green, Figure 3) is plotted between corresponding 95% confidence limits for the U-series ages. For the interval between 34.15 and 45.03 in CU1-1, the mean age model growth rate ranges between 1.44 and 1.89 mm/kyr, whereas for the interval between 45.04 and 49.99 kyr BP ranges between 1.90 and to 6.51 mm/kyr.

4.2 Trace elements (TE)

Figure 5 shows a selection of trace element time-series analyzed in CU1-1. Using Pearson's correlation, we measured the correlations between pairs of the TE/Ca concentration data (Figure 6a). Because the individual TE/Ca time series showed autocorrelation greater than 0.5 p-values were corrected by reducing the degrees of freedom in our t-statistic test calculations (Figure 6b). Trace element results are described by grouping positively correlated TE/Ca variables together. The maximum and minimum values of each TE/Ca can be assessed from Figure 5.

Group I: S/Ca, Na/Ca, U/Ca, P/Ca

S/Ca, Na/Ca, U/Ca and P/Ca show a positive correlation with correlation coefficient R ranging from 0.3 to 0.7 that is statistically significant (p-value <0.02) (Figure 6).

Group II: Mg/Ca and Sr/Ca

Mg/Ca and Sr/Ca show a strong positive correlation (r = 0.5) that is statistically significant (p-value < 0.005). Results of bivariate data analysis between the two variables in log space shows a linear regression of the data, with a positive slope of ~0.7 and stronger, significant correlation (R = 0.6, p-value <0.01) (Figure 8). Mg/Ca shows the highest average concentration in the stalagmite.

Group III: Al/Ca and Si/Ca

Al/Ca and Si/Ca show a positive correlation (r = 0.3) that is significant (p-value <0.01). Trace element analysis revealed that both Al/Ca and Si/Ca have relatively low average concentrations in CU1-1 (1.66 and 0.85 mm/mol, respectively).

Group I and Group II are anticorrelated. Trace element results show negative correlation between Mg/Ca and Sr/Ca relative to S/Ca, Na/Ca, U/Ca, P/Ca. Al/Ca and Si/Ca ratios show weak positive correlations with Na/Ca, S/Ca, P/Ca (r = 0.3) that are significant (p-value <0.02) with the exception of Al/Ca vs S/Ca (p-value = 0.1) and Si/Ca vs Na/Ca (p-value = 0.06) which showed statistically insignificant results. Al/Ca and U/Ca ratios show almost no correlation (r = 0.04) that is insignificant (p-value = 0.1).

Ba/Ca does not fall into this grouping scheme. Bivariate data analysis showed Ba/Ca to be positively and significantly correlated to Group II with correlation coefficient r ranging from 0.3 to 1, and negatively correlated with Groups I (p-value < 0.01) and III (p-value = 0.1) with correlation coefficients ranging from -0.1 to -0.4.

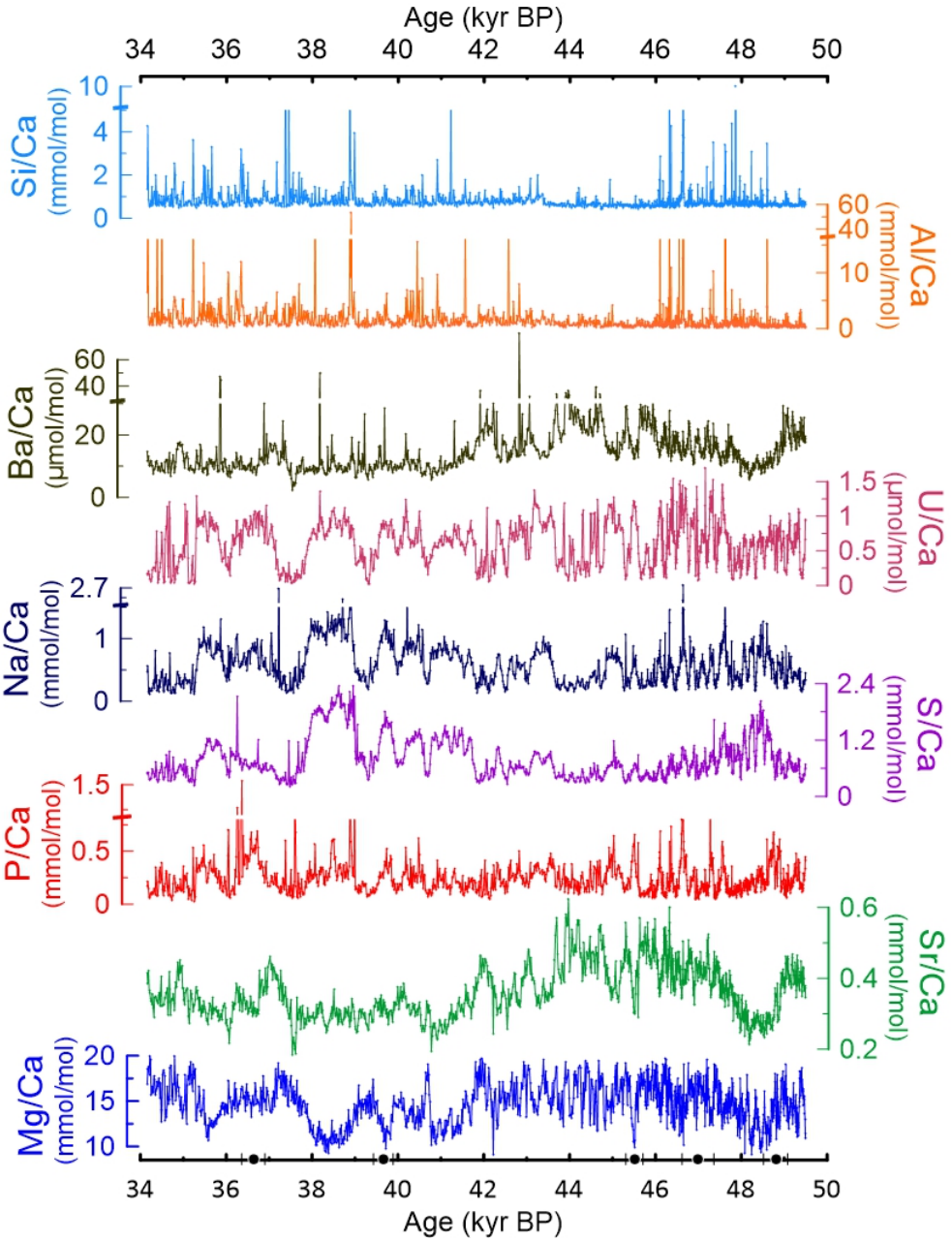

Figure 5. Trace element calcium concentration (mmol/mol) and (µmol/mol) time series in CU1-1 (34-50 kyr BP): Black markers along the x-axis are U-Th age control points, uncertainty ranges between ± 0.2 and 0.37 kyr BP.

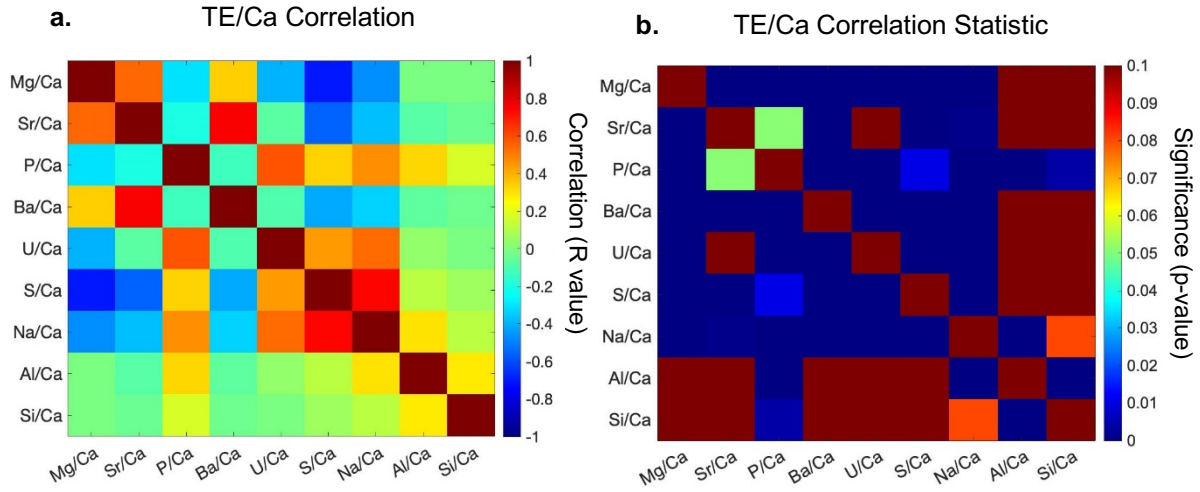

Figure 6. Pearson Correlation Coefficient Matrix of trace element (TE)-to-calcium ratios and their associated statistical significance: shown on the left (a) is the correlation coefficient color plot for TE/Ca. Dark red represents a positive correlation (R = 1), light green represents no correlation (R= 0), dark blue represents a negative correlation (R = -1). Shown on the right (b) is color plot of associated correlation coefficient p-values. P-values for the data range from 0.1 – 0.01.

4.3 Stable Isotope $\delta^{18}O$ and $\delta^{13}C$

Isotopic compositions of oxygen and carbon in calcite ($\delta^{18}O$ and $\delta^{13}C$) were analyzed at a 100-µm resolution (n = 332 samples). The $\delta^{18}O$ and $\delta^{13}C$ values range between -13.44 and -5.56‰ and between 1.39 and -6.48‰, respectively (Figure 7a). The $\delta^{18}O$ record shows two anomalous data points at 36.77 (kyr BP) and 40.38 (kyr BP), as compared to their adjacent data points. We consider these values outliers. The data are shown in our stable isotope time series as discontinuous points (Figure 7a).

High $\delta^{18}O$ values occur within multiple time windows in our record: ~35.6–36.2, ~38.0–38.8, 40.8–41.0 and 48.0–48.4 kyr BP. Relatively high $\delta^{13}C$ values occur within the same time windows. Both $\delta^{18}O$ and $\delta^{13}C$ show the heaviest isotopic values during the time windows 35.6–

36.2 and 48.0–48.4 kyr BP. Bivariate analysis of the stable isotope date shows $\delta^{18}O_{calcite}$ and $\delta^{13}C_{calcite}$ are positively and significantly correlated (Figure 7b). Cross correlation between the stable isotope data and TE data show that Mg/Ca and Sr/Ca are negatively and significantly correlated with $\delta^{18}O$ and $\delta^{13}C$ (Figure 9).

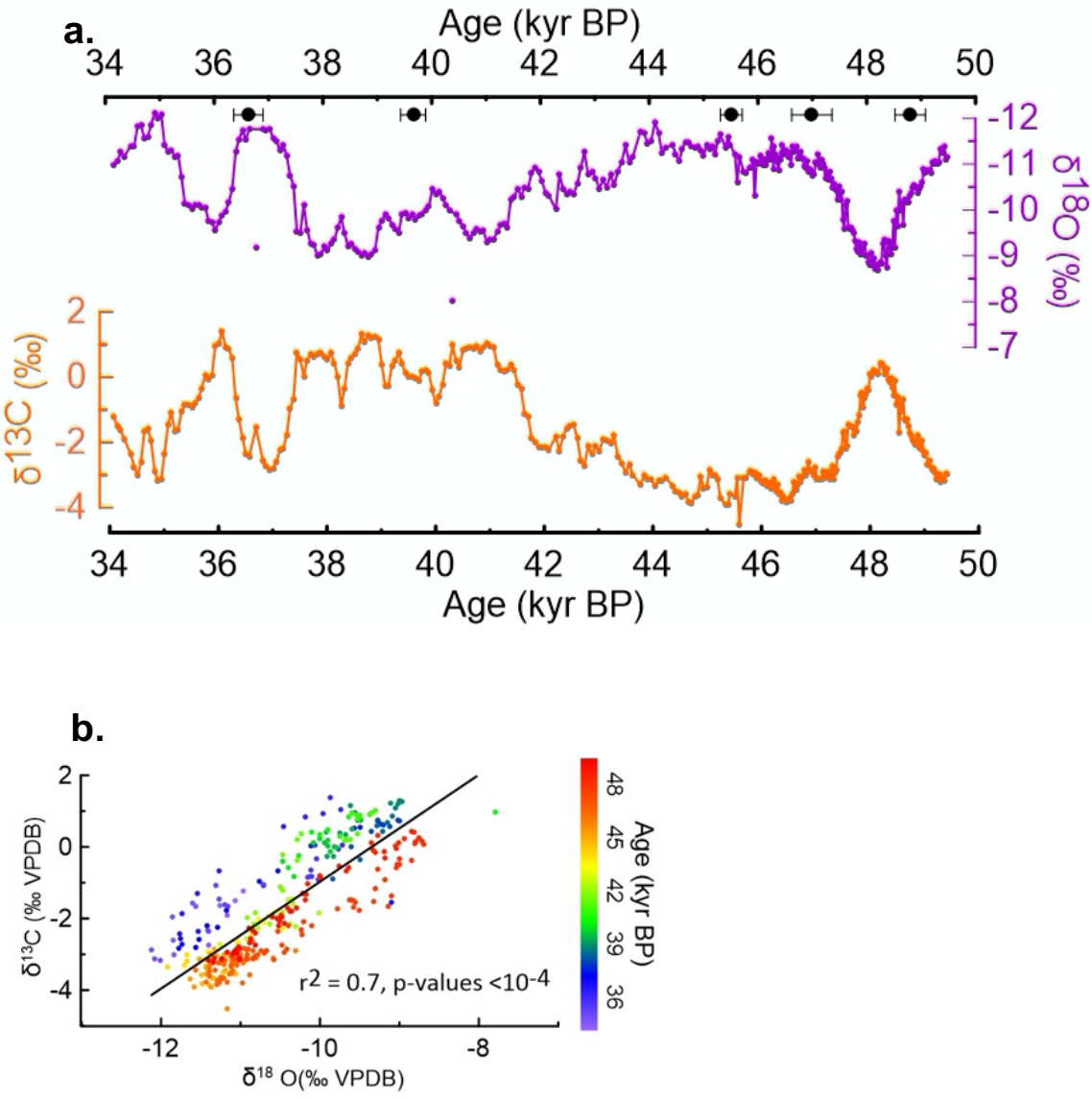

Figure 7. a. $\delta^{18}O_{calcite}$ and $\delta^{13}C_{calcite}$ time series. Age control points and uncertainty (2σ) are indicated along the top x-axis. **b.** $\delta^{18}O_{calcite}$ and $\delta^{13}C_{calcite}$ correlation. The color bar indicates the age of each data point (34-50 kyr BP).

5. Discussion

5.1 Trace Element Incorporation

The incorporation of trace elements into stalagmites from drip water occurs as minor components of carbonate precipitating from solutes and or as inclusion of aluminosilicate colloids (particles) stemming from the soil washout above the cave. Colloids are defined as matter ranging between 1 nm and 1 μm, largely consisting of aluminosilicate minerals with Al, Si, Mg, and Fe as major constituents (Lead and Wilkinson, 2006). Solutes consist of dissolved elements and molecules or hydrated ions (Lead and Wilkinson, 2006). Given the relatively low concentrations of Al/Ca and Si/Ca (Figure 5) and negative correlation of Al/Ca and Si/Ca with Mg/Ca and Sr/Ca (Figure 6), we conclude that Mg/Ca and Sr/Ca incorporation into CU1-1 is not driven by the same mechanism(s) as those governing Al/Ca and Si/Ca incorporation into calcite.

5.2 Temperature and growth rate

Trace element incorporation in calcite from solutes are primarily controlled by temperature, growth rate, drip water rate (Fairchild and Treble, 2009) and fluid mixing (Day and Henderson, 2013). The Mg/Ca values of our sample show a long-term variation from ~9 to 19 mmol/mol and short-term variation from ~13 to 19 mmol/mol, a change in concentration by 111% and 46%, respectively, relative to the lowest value within each range (Figure 4). According to experiments that mimic cave conditions (Day and Henderson, 2013), Mg/Ca increases by ~2% per 1°C. Consequently, if the largest observed increase of Mg/Ca from ~ 9 to 19 mmol/mol were caused solely by temperature change, it would require a regional temperature change of 37ºC. The short-term variation where Mg/Ca change from ~13 to 19 mmol/mol would require

a regional temperature change of 18ºC. Northern high latitude records reveal the largest temperature change experienced in the northern high latitudes during the time interval represented by CU1-1 (34-50 kyr BP) was ~16.5ºC (Kindler et. al., 2014). Therefore, we assume that calcification temperature is not the only mechanism driving Mg/Ca incorporation into the stalagmite with the exception of intervals like ~37-39 ky BP where Mg/Ca and Sr/Ca do not co-vary, rather Mg/Ca values decline whereas Sr/Ca values remain relatively unchanged. This discrepancy may be the result of other mechanisms overprinting cave drip water chemistry interactions, such as large changes in temperature within the cave system.

The partitioning of a TE between a carbonate species and aqueous solution is generally represented by the distribution (or partition) coefficient, K_d, which is defined as the ratio of the quantity of the adsorbate absorbed per mass of solid to the amount of the adsorbate remaining in the solution at equilibrium (Rimstidit et al., 1998). Practical TE partitioning into $CaCO_3$ can be understood as $K_d = (TE_{solid} / Ca_{solid}) / (TE_{aqueous} / Ca_{aqueous})$ were the solid is the stalagmite and aqueous is the dripwater solution. The partition coefficient of a TE will therefore determine the likelihood at which it will become incorporated into the solid or in our case the $CaCO_3$ stalagmite. Laboratory experiments can quantify the rate of TE incorporation of a given element based on its K_d value.

In contrast to Mg/Ca concentration, laboratory experiments indicate that Sr/Ca does not show a significant temperature dependency within a range of 7-35 ºC (Day and Henderson, 2013). Day and Henderson (2013) suggest that realistic changes in stalagmite growth rates ($\leq$ 1 mm/kyr) have no noticeable effect on Sr incorporation into calcite, even over a relatively large

increase in growth rate range (0.97 mg/day to 7.70 mg/day). In contrast, other studies suggest that strontium partitioning into calcite is sensitive to growth rate (Mucci and Morse, 1983; Tesorio and Pankow, 1996; Huang and Fairchild, 2001). However, Fairchild and Treble (2009) point out that the previous studies in support of growth rate as a dominant mechanism for trace element incorporation, showed K_dSr changes by 15 to 30 % for an order of magnitude of growth rate increase. In our stalagmite segment the average growth rate is of 2.7 mm/kyr (ranging between 1.4-6.5mm/kyr) for the entire time interval (34-50 kyr BP). Growth rates remain relatively steady ranging between 1.4-1.7 mm/kyr from 34 - 42 kyr BP. During the following 2 kyr interval 42-44 kyr BP, growth rate decreases from 1.6 to 1.4 kyr BP, followed by a sharp increase within 44-46.5 kyr BP where the average growth rate is ~3.5 mm/kyr ranging between 1.5 and 6.5 mm/kyr. The growth rate steadily levels off, remaining relatively constant (3 mm/kyr) through the end of our record. Considering the interval of greatest change, 44-46.5 kyr BP, CU1-1 does indeed fall within Day and Henderson (2013**)** proposed growth rate range affecting K_dSr incorporation. Deeper in the record, Sr/Ca shows a proportionally stronger response than Mg/Ca from 42 to 47 kyr BP. This divergence may be due to strontium's dependance on growth rate (Day and Henderson, 2013).

Sr/Ca and Mg/Ca show a strong covariation for most of the record (Figure 5). However, between the interval of ~37.5 and 38 kyr BP Mg/Ca shows a proportionally stronger change than Sr/Ca. This may be due to the influence of temperature on Mg/Ca incorporation in the stalagmite, making Mg/Ca more sensitive than Sr/Ca. The partition coefficient of magnesium (K_dMg) is temperature-dependent (Gascoyne, 1983; Huang and Fairchild, 2001; Sinclair et al., 2012) and increases by ~2% per 1°C. Therefore, K_dMg, may vary within local conditions (i.e.,

extreme seasonality, glacial transitions) resulting in speleothem chemistry that is impacted by variations in cave temperature.

In summary, CU1-1 Sr/Ca data do not always share the major trends evident in the Mg/Ca data (Figure 4), indicating that there are time intervals during which temperature and growth rate may play a role in co-shaping Mg/Ca and Sr/Ca trends in our stalagmite, respectively. According to experiment results by Day and Henderson (2013), Mg/Ca shows temperature dependency, though only if large temperature change (~25ºC) is considered. In contrast, the incorporation of Sr/Ca does not reveal a relationship to temperature. Co-variation between Sr/Ca and Mg/Ca in CU1-1 is likely due to changes in drip rate which is related to the amount of precipitation above the cave. Thus, intervals of co-variation between Mg/Ca and Sr/Ca (Figure 5) likely indicate that temperature and growth rate did not exert a dominant control on trace element incorporation into calcite.

Two notable periods of decreased Mg/Ca and Sr/Ca concentration occur between ~38-39 kyr BP and ~48-49 kyr BP. Both Mg/Ca and Sr/Ca show relatively lower concentrations in the first half of the record spanning 34-42 kyr BP and maintain higher concentrations thereafter (42-47 kyr BP) until they synchronously decline at the end of the record (~47-49 kyr BP). The positive and statistically significant correlation between Mg/Ca and Sr/Ca (Figure 5) implies that the incorporation of Mg and Sr into the calcium carbonate stalagmite is largely driven by common mechanism(s). We interpret this reflect a fluid-dominated pattern in which the trace element to calcium ratio is likely controlled by changes in calcium precipitation and drip rate–directly corresponding to the amount of rainfall over the cave.

5.3 Contribution of P, Al, and Si

To understand which mechanisms control P incorporation, we analyzed the relationship between Al/Ca and P/Ca which shows a positive and significant correlation (Figure 6). CU1-1 data show an average Al to P ratio of 6.5 (ranging from 0.30-97), which is much lower than the average ratio in bulk continental crust (Al/P =193) (Rudnick and Gao, 2003). The comparison demonstrates that we have a substantially higher amount of P relative to Al in our sample. Assuming a congruent chemical weathering, aluminosilicates are not the sole source of P in our stalagmite.

P/Ca is anticorrelated with both Mg/Ca and Sr/Ca (Figure 5 and 6). Notable periods of increase P/Ca concentration occur between 35–36, 36-36.5, 37.5-39, and 48- 49 kyr BP, corresponding to a decrease in Mg/Ca and Sr/Ca. We can therefore assume that P is sourced and incorporated into the stalagmite through a different mechanism than that of Mg/Ca and Sr/Ca. A potential source for P in CU1-1 may be from degradation products of organic matter washed out from the soil cycling above the cave (PO_4^{-3}) and incorporated into cave drip water solution as particles. If the source of P is soil washouts form above the cave, we interpret the concentration of P/Ca within CU1-1 to reflect the hydroclimate above the cave: high and low P/Ca values reflecting wet and dry climatic periods, respectively.

Having excluded the inclusion of aluminosilicates, anomalously high calcification temperature, and anomalous growth rate as the dominant factors of Mg and Sr incorporation, we hypothesize that Prior Calcite Precipitation (PCP) that is driven by degassing is the most likely dominant mechanism for Mg and Sr incorporation in CU1-1. PCP refers to the calcite precipitated out of flow water within the karst system above the cave prior to reaching the

stalagmite. Before infiltrating a cave, rain water percolates through vegetated epikarst and soil containing CO_2 as products of a microbial decomposition of organic matters. Water entrains CO_2 gas from the soil into the underlying saturated zone. Enriched in dissolved CO_2, the water is now a weak acid (H_2CO_3) which readily dissolves calcium carbonate rock within the roof of the cave. Upon entering the cave, reduced pCO_2 in the cavern results in a strong pressure gradient between that of the water and the cave, initiating CO_2 degassing and subsequent calcite precipitation in karst system above the cave floor. Relatively pure calcite is preferentially precipitated out of solution, lowering Ca concentration in the flow water and relatively increasing the incompatible elements with partition coefficients (K_d) less than 1 (i.e., Mg, Sr, Ba, P, U). PCP is controlled by cave water drip rate which is a function of the amount of precipitation occurring over a cave (Fairchild and Treble 2009; Fairchild et al., 2000; Tooth and Fairchild, 2003). PCP is strongest when drip water rate is low during a dry season or sustained drought (Sinclair et al., 2012, Day and Henderson 2013). Slow drip water rate allows more time for degassing to occur. Enhanced degassing of the drip water solution results in greater amounts of calcite to precipitate out of the drip water solution, leaving the drip water enriched in trace elements such as Mg and Sr. Thus, Mg and Sr concentrations in stalagmite layers are generally low if formed during a prolonged wet period, as demonstrated in multi-year cave drip water and stalagmite studies (Fairchild and Treble 2009).

5.4 Evidence for prior calcite precipitation

$CaCO_3$ formation of our stalagmite is dependent on the cave drip rate and the degree of PCP. Stalagmites which form under PCP forming conditions generally exhibit a strong positive correlation between ln (Mg/Ca) and ln (Sr/Ca) in drip-waters and $CaCO_3$ (Sinclair et al., 2012;

Fairchild and Treble, 2009; Tooth and Fairchild, 2003). The linear fit of ln (Sr/Ca) and ln (Mg/Ca) data in our stalagmite shows a positive correlation with a slope of 0.7, falling within the envelope for PCP driven trace element incorporation (Figure 8). The co-variation of ln (Sr/Ca) and ln (Mg/Ca) in our stalagmite indicates Mg and Sr share a common mechanism for incorporation, PCP. If the drip rate and degree of PCP are directly correlated to the amount of rainfall occurring over the cave, then we are able to use Sr/Ca and Mg/Ca concentrations as proxies for rainfall reconstruction.

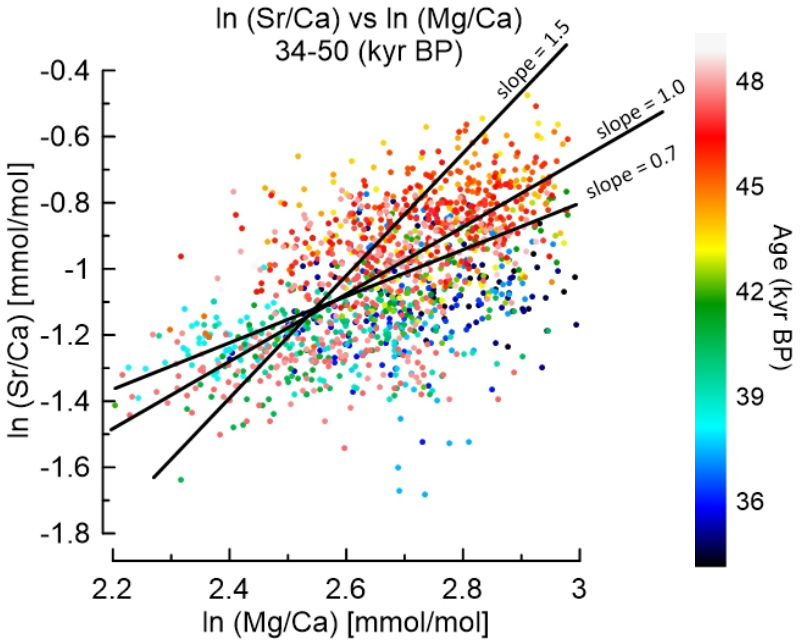

Figure 8. ln (Sr/Ca) vs ln (Mg/Ca) correlation: the data shows a comparison to Sinclair et al., (2012) slope ranges (m = 1.02–0.7) for stalagmite growth and trace element incorporation driven by PCP. The black line is a linear fit of the TE data from CU1-1. The color bar indicates the data range in ages (34-70 kyr BP).

5.3 The relationship between $\delta^{18}O$, $\delta^{13}C$ and select trace elements

The $\delta^{18}O$ and $\delta^{13}C$ values of stalagmite calcite are shaped by multiple processes and mechanisms that are challenging to disentangle from each other. Changes in $\delta^{18}O$ of stalagmites likely reflect a combined effect of changes in the rainfall amount, moisture source, precipitation temperature, and processes that occur within the cave environment (i.e., partial pressure of CO_2 and degassing of water within the karst system) (Lachniet et al., 2009).

Changes in $\delta^{13}C$ values in stalagmites reflect a number of processes that occur in the soil above the cave and interaction of water and karst rock within the cave system. Dominant mechanisms that shape the $\delta^{13}C$ of stalagmites are: i) vegetation development and cover, the ratio of C_3 and C_4 vegetation above the cave and the amount of microbial degradation of organic matter (CO_2 release) in the soil above the cave, and ii) water and karst rock interaction and degassing of water in the karst system driven pCO_2 (Day and Henderson, 2011).

Kinetic processes could have potentially led to the observed stable isotope values in CU1-1 and drive $\delta^{18}O$ ($\delta^{13}C$) to higher values (PCP, temperature and moisture source). In the case of the stable isotope, an increase in precipitation over the cave (increased drip rate) would result in heavier stable isotope values owning to less CO_2 degassing (PCP). The initial source of carbon for stalagmites is from the CO_2 present in the soil, mainly provided by plant respiration and decomposition of organic matter. Upon contact with water, it forms carbonic acid in which dissolves cave host-rock. There for the $\delta^{13}C$ values are affected by the amount of CO_2 in the soil-vadose zone and the moisture source of the dripwater. The $\delta^{13}C$ values of soil-respired CO_2, vary depending on the precipitation and organic matter respiration. Decreases in soil respiration rate may result in elevated soil CO_2 and hence heavier $\delta^{13}C$ values. Therefore, the moisture source of the dripwaters may influence $\delta^{13}C$ values if the water is coming from a region with relatively high atmospheric pCO2, a feature of CAM plants–Crassulacean acid metabolism plants which minimize photorespiration and save water by separating these steps between day and night– which is well recorded in cave deposits (Breeker et al., 2017).

We infer dominant factors that shaped the temporal variation of $\delta^{18}O$ by examining the relationship between $\delta^{18}O$, $\delta^{13}C$ and trace elements. $\delta^{18}O$ and $\delta^{13}C$ in CU1-1 show a strong positive correlation that is statistically significant ($r^2 = 0.7$, p-value $<10^{-4}$) throughout the record (Figure 7b and Figure 9). There are at least three mechanisms that could explain the strong $\delta^{18}O$ and $\delta^{13}C$ covariance in our sample.

The first mechanism is changes in degassing and therefore PCP within the karst system. Both $\delta^{18}O$ and $\delta^{13}C$ values of the precipitated $CaCO_3$ depend on the isotope composition of the dissolved carbonate species. Degassing of CO_2 from a solution with a relatively high pCO_2 in the karst system leads to the enrichment of $\delta^{13}C$ in residual dissolved inorganic carbon (DIC). Once the solution is oversaturated in dissolved calcium, kinetic fractionation effects cause the dripwater solution to preferentially precipitate out the heavier $\delta^{13}C$ species into the karst system and the stalactite *prior* to reaching the stalagmite. The impact between the dripwater solution and the stalagmite surface results in further degassing and, as a result, calcite precipitation. In other words, the degassing of isotopically light CO_2 and isotopically heavy $CaCO_3$ precipitation in the karst system is what leaves the stalagmite low in $\delta^{13}C$ during periods of enhanced degassing, and vice versa. This scenario is consistent with the Mg/Ca and Sr/Ca trends as well. During H4 and H5 both trace element records show a relative decrease with low $\delta^{18}O$ and $\delta^{13}C$ values. In summary, the Mg/Ca and Sr/Ca trends confirm a wet phase over the cave which drives $\delta^{18}O$ and $\delta^{13}C$ to low values due to a weakening in the degassing/PCP effect.

The second mechanism attributes variations in $\delta^{18}O$ and $\delta^{13}C$ to the moisture source (precipitation) and vegetation above the cave, respectively. The data shows that $\delta^{13}C$ and $\delta^{18}O$

values range from -2 to 3‰ and -12 to -8‰, respectively (Figure 7a). Average $\delta^{13}C$ isotope signatures for C_3 plants range from -27 to -29‰ and for C_4 plants range from -12 to 16‰, thus we conclude that the $\delta^{13}C$ signature in CU1-1 is not dominantly modulated by the product of microbial decomposition of organic matters of either plant type. When analyzing the temporal and spatial distribution of the stable isotope composition of ($\delta^{18}O_{precipitation}$) precipitation in this region during our record (34-50 kyr BP), we would expect relatively light $\delta^{18}O$ values ranging from -6 to -9‰, if the moisture source was indeed from the Asian Monsoon (Patusata et al., 2011; Yao et al., 2013; Hren et al., 2009) because local processes affect the isotopic composition of precipitation. Moisture sourced from the Asian monsoon would have to cross over significant topographic boundaries such as the Himalayan Mountains to reach the site. Following Rayleigh distillation, this would result in greater isotope fractionation carrying a lighter $\delta^{18}O_p$ later incorporated into the stalagmite carbonate. However, a $\delta^{18}O_{precipitation}$ - enabled simulation study suggests $\delta^{18}O_{percipitation}$ values during Heinrich Event 1 are expected to be heavier over Central Asia relative to the Last Glacial Maximum (Pausata et al., 2011) (enrichment by 0.9 to 1.7‰) due to non-local processes effecting isotopic composition of precipitation. Consequently, the monsoon scenario and vegetation changes are unlikely to explain the observed trend of $\delta^{18}O$ and $\delta^{13}C$ in CU1-1.

The third and most likely explanation for $\delta^{18}O$ and $\delta^{13}C$ covariance and relatively heavy isotopic values is that they both reflect kinetic fractionation effects of degassing and PCP (Figure 7 and Figure 9). The $\delta^{18}O$ signature may also reflect changes in moisture source which depends on rainfall temperature, with heavier $\delta^{18}O$ values owning to higher temperatures. An isotope-enabled climate model for the $\delta^{18}O$ controls of a Chinese stalagmite during a simulated

Heinrich event (Pausata et al., 2011) showed heavier $\delta^{18}O$ values relative to the Last Glacial Maximum. The H1 simulation resulted in cooling of the Indian Ocean, causing a reduction in rainfall over the Indian Ocean and Indian sub-continent and heavier δ18O over northern India. Heavy $\delta^{18}O$ values in the Chinese stalagmite were therefore interpreted to reflect non local processes. Pausata et al (2011) propose two non-local processes which drive $\delta^{18}O$ to heavier values, both of which are plausible processes contributing to the relatively heavy $\delta^{18}O$ in CU1-1. The first process is a change in the source of the water vapor that is delivered to the cave, owning to changes in atmospheric circulation. The second process is a change in the fractionation of $\delta^{18}O$ in the water vapor during transit to the cave.

For most of the record, $\delta^{18}O$ and $\delta^{13}C$ are negatively correlated with Mg/Ca and Sr/Ca (Figure 9) (r = -0.4 for $\delta^{18}O$ and $\delta^{13}C$ vs Mg/Ca; r = -0.6 for $\delta^{18}O$ and $\delta^{13}C$ vs Sr/Ca). However, when considering the time-variant correlation within a 1-kyr time window, Mg/Ca and $\delta^{18}O$ show a positive correlation in the beginning of the record at 34.7 kyr BP and during 45.7-47.7 kyr BP, coincident with the timing of D-O stadials and H5 events (Figure 9, 10). As previously discussed, the Kd_{Mg} is affected by temperature within a certain range (7-35ºC). Considering the magnitude of temperature change experienced in the North Atlantic within the length of our record (6.5 to 16.5ºC, Kindler et al., 2014), and changes in the fractionation of $\delta^{18}O$ at the moisture source–owing to changes in North Atlantic SST–we conclude that temperature impacted the $\delta^{18}O_p$ and Mg/Ca signatures. Interestingly Sr/Ca and $\delta^{18}O$ data show strong correlations at intervals 36.7, 38.7, and 45.7-46.7 kyr BP, coincident with the timing of H5 and D-O stadials (Figure 9, 10). The $\delta^{18}O$ and $\delta^{13}C$ show weaker positive correlations during H4 and H5 time windows (38-40, 47-49 kyr BP, respectively). As discussed above, we interpreted

the strong correlation and co-variance between Mg/Ca and Sr/Ca to reflect changes in degassing and PCP that, in turn, is driven by changes in drip rate. We hypothesize that the negative correlation between the stable isotope data and Sr/Ca and Mg/Ca values indicates PCP (degassing) as the dominant processes that shaped the element and isotope in the TE data. Dry phases are manifested in high Mg/Ca and Sr/Ca, low P/Ca, and low values of $\delta^{18}O$ and $\delta^{13}C$. The opposite is true during a wet phase.

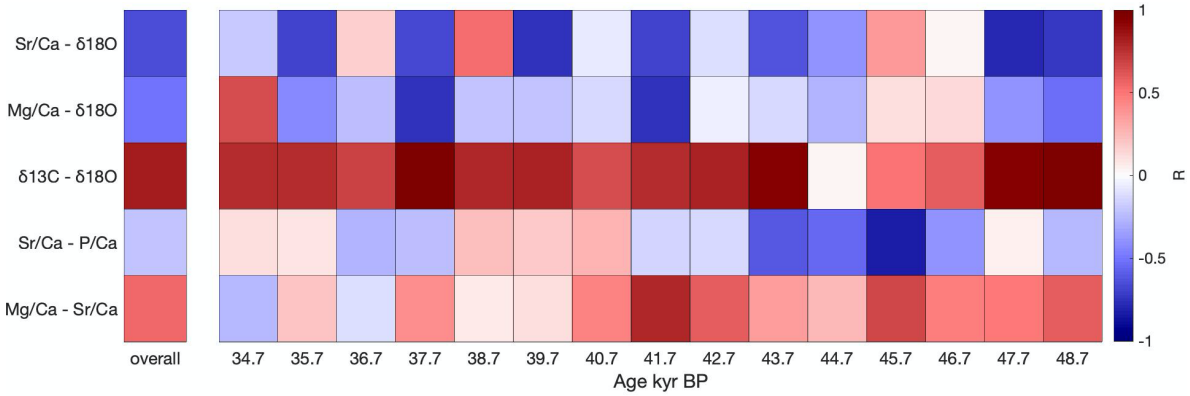

Figure 9: Stable isotope and trace element time variant correlation in CU1-1. Correlation coefficient (p) for Pearson's rank correlation tests overall (first 1 x 5 matrix) and on a 1 kyr-long windows (second 15 x 5 matrix) for Mg/Ca, Sr/Ca and $\delta^{18}O$ and $\delta^{13}C$ data measured in CU1-1. The color bar on the far right indicates the correlation strength: red is a strong, positive correlation; blue represents a weak, negative correlation; white represents no correlation.

5.4 Spectral Analysis: identifying trends within the TE data series

We evaluated variation between our Mg/Ca and Sr/Ca records using cross wavelet analysis with data sampled on a 20-year time step (Figure 10). This technique simultaneously analyzes spectral features of Mg/Ca and Sr/Ca to describe their temporal evolution (Grinsted et al., 2004). The analysis shows high common power in the 0.25-0.50 kyr band from 41-48 kyr. We interpret the short-term variability to reflect sensitivity to climate changes over our cave site. It is difficult to ascribe short-term variability in our analysis to climate events in the North Atlantic for two reasons: the duration of D-O oscillation (~1.50 and 0.64 kyrs) and the higher

resolution of our record relative to the North Atlantic climate records. These uncertainties pose the potential for other climate modes.

Results also show high common power in the 2-3 kyr band which corresponds to H4. Another prominent wet phase at the end of our record (45–49 kyr BP) does not fall within the cone of influence (COI, Figure 10) making it difficult to confidently interpret the climate signal in the 2-3 kyr band over 45– 49 kyr BP. However, this time window does correspond to H5 which is reflected in our TE and stable isotope data (Figure 5 and Figure 7a).

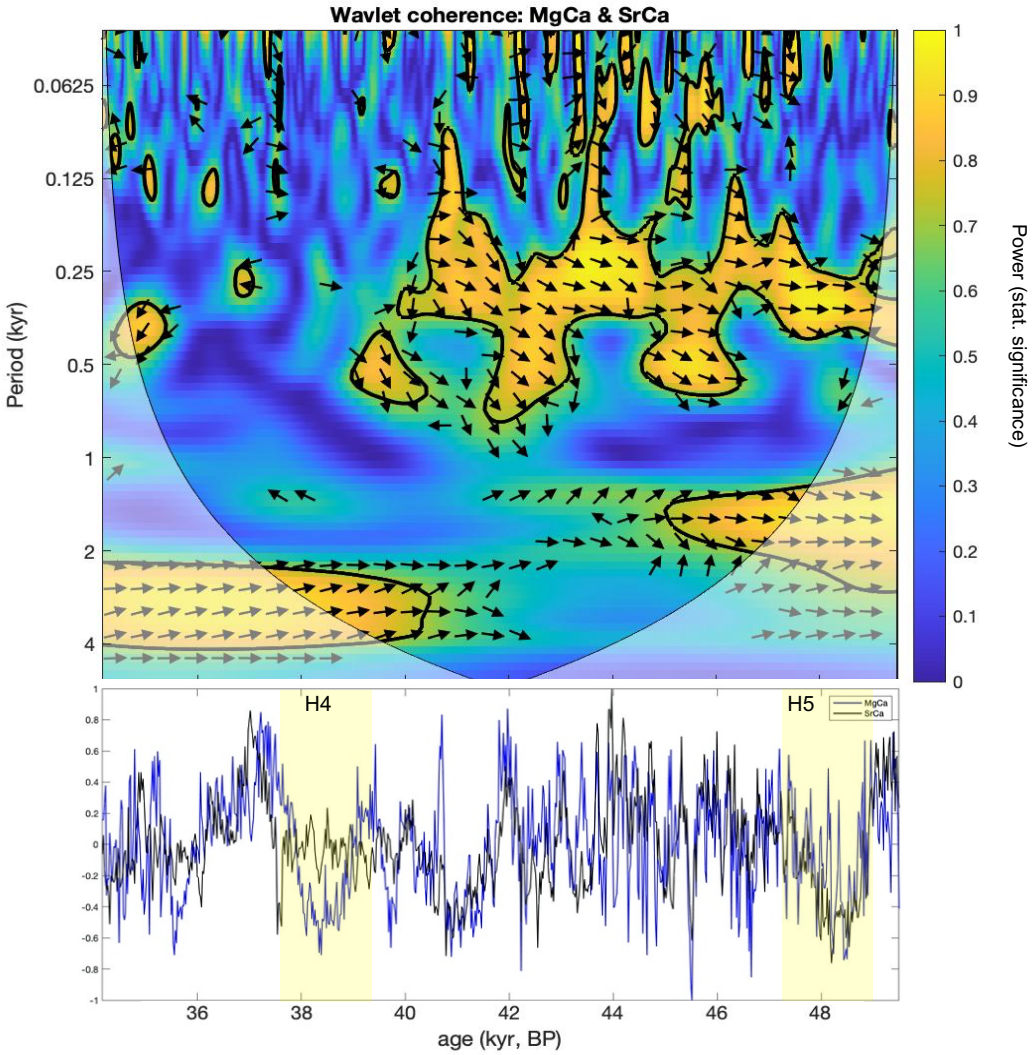

Figure 10. Cross wavelet coherence between the standardized Mg/Ca (blue) and Sr/Ca (black) time series (bottom). The standardized series has a first order autoregressive (AR1) coefficient

< 0.5. The 5% significance level against red noise is shown as a thick contour and the cone of influence (COI) where edge effects might distort the picture is shown as a lighter shade. The relative phase relationship is shown as arrows (with in-phase pointing right, anti-phase pointing left). All significant sections show in-phase behavior. General window for H4 and H5 are highlighted in the standardized data plot (bottom). Methods used for wavelet coherence analysis are adapted from Grinsted et al., 2004.

5.5 Potential link between northern hemisphere high and mid latitude climates

Our record reveals centennial–millennial scale variability. As discussed in the previous section, it is difficult to ascribe each mode of variability in our record to North Atlantic climate events recognized in Greenland ice core records. Considering individual age model uncertainties, the patterns in our stalagmite data capture climate changes during Heinrich events (Figure 11). We interpret wet phases as Mg/Ca and Sr/Ca values that are significantly lower than the average and P/Ca values that are higher than the average. During H4 (38-40 kyr BP) and H5 (47-49 kyr BP) our trace element time-series show a decrease in Mg/Ca and Sr/Ca and an increase in P/Ca relative to their averages (14.7, 0.36, 0.24 mmol/mol, respectively) within age uncertainties ($\pm$ 0.37 kyr and $\pm$ 0.28 kyr, respectively). For the PCP mechanism, relatively low Mg/Ca and Sr/Ca suggest increased drip rates and by extension, increased rainfall over the cave. During the same intervals our $\delta^{18}O$ and $\delta^{13}C$ time series show heavier values due to PCP, moisture source, and temperature effects. Therefore, we infer wet periods over Central Asia in response to freshwater induced cooling in the North Atlantic during H4 and H5 (Figure 11).

Shorter scale variability within our record may reflect D-O oscillations. Within the length of our record six D-O oscillations have been previously documented in Greenland ice core data: GI-8 to 13 and GS-9 to 14, interstadial and stadial events (Bjork et al., 1998). Our Mg/Ca, Sr/Ca, P/Ca, $\delta^{18}O$ and $\delta^{13}C$ data suggest that prominent wet periods over the study site may coincide with the timing of D-O stadials. Based on the GRIP SS_{09} time scale our record may

align with 4 of the 6 D-O stadials: GS-10 (38,311 kyr BP, duration 0.64 kyr); GS-11 (39.671 kyr BP, duration 0.680 kyr); GS-12 (41,811 kyr BP, duration 0.960 kyr); and GS-14 (47,011 kyr BP, duration 0.260 kyr). Interestingly the D-O evets potentially reflected in our stalagmite are relatively short lived as compared to the average D-O stadial duration. The duration and strength of each stadial may therefore play a role in the magnitude of precipitation variability over the cave.

Our data also indicate several wet episodes that do not correspond with D-O stadials. For example, intervals 35.5-36.0, 42.0-42.3, 43.2-43.5, 46.8-47.0 kyr BP show high P/Ca, low Mg/Ca and Sr/Ca values relative to their respective averages and heavy $\delta^{18}O$ and $\delta^{13}C$ values, suggesting a wet phase over our cave site however, do not align with any known D-O stadials. Conversely, not all D-O stadials, clearly align with a wet interval over our cave. Assuming age model uncertainties are not responsible for the misalignment between wet phases in Central Asia and the imprints of D-O stadials, suggests that other climate modes exert a strong control on precipitation over our cave site (Figure 11).

Due to temporal alignment of H4 and H5 with wet phases over our study site we hypothesize that Central Asia's hydroclimate is linked to the North Atlantic climate by atmospheric connections. Climate patters such as the North Atlantic Oscillation, East Atlantic/West Russian pattern and Atlantic Multi-decadal Oscillation (AMO) have previously been linked to Central Asia's winter precipitation variability (Geriltz et al., 2018; de Beurs et al., 2018, Swann et al, 2005). A dominant source for winter precipitation over Central Asia, including our study site, is associated with seasonal shifts of the mid-latitude Westerlies which follows the annual cycle

of insolation and heating (Figures 1a and 1b) (Aizen et al., 2001; Bothe et al., 2011; Schiemann et al., 2008, 2009). In winter, the jet is located father south and our cave site receives most of its moisture from the southwest. During spring, the position of the jet allows for zonally oriented wave patterns across North Eurasia, causing storms in south Central Asia and increasing the Westerly moisture supply. In the summer, Northern Hemisphere monsoon moisture is sourced from farther northward of the wave track, as compared to winter. The net effect of the high- and low-pressure gradient pattern created during winter causes an increased south-westerly flow, enhancing transport of moisture from the Mediterranean, Aral and Caspian Seas into Central Asia (Aizen et al., 2001). Another dominant mechanism for moisture transport to the region is the Siberian High–cold air that accumulates over northeastern Eurasia from September until April. Using Central Asia's primary moisture transport circulation tracts, below discuss potential atmospheric circulation patterns which may have caused an increase in precipitation over our cave site during H4 and H5.

The characteristic directions of westerly winds and distribution of precipitation for positive and negative NAO phases provide a possible teleconnection mechanism between the North Atlantic and Central Asia. Positive NAO anomalies cause a strengthening of the westerly winds over Central and Norther Europe causing on a northern trajectory towards Central Asia. This circulation pattern should weaken the Siberian High (Gong et al., 2001, Gong and Ho, 2002) and prevent dry, cold Arctic air from reaching Central Asia causing relatively wet winters in southwestern Central Asia–this is where our cave site is located. A negative NOA phase causes a southward shift in the Westerly winds and allows cold, dry Arctic air from the Siberian High to reach far southwards into Central Asia (Seyd et al., 2010) resulting in dry

winters over out study site. For the negative NAO scenario, moisture would likely be sourced from warmer temperature regions such as the Mediterranean, Aral, and Caspian Seas and should be reflected in the δ18O as heavier values.

Another important wind system, affecting the moisture transport to Central Asia is the East Atlantic/West Russian pattern (EA/WR) (de Beurs, 2018; Geriltz et al., 2018). It is driven by a pressure gradient over Western Russia which forms a dipole of high (low) pressure over western Europe (Russia), determining the strength and position of the Siberian High. Favorable conditions for winter precipitation development over our cave site occur when the Siberian High is positioned further to the east, as opposed to the west (Azien et al, 2001; Ding et al., 2004, Gong et al., 2002). An eastward shift generally occurs during a negative phase of the EA/WR patter with low pressure over Europe. Stationary wave models show that EA/WR pattern is found to be closely associated with the stationary manifestation of Rossby waves over the Atlantic Ocean (Lim 2015). This pattern suggests that the EA/WR reflects Rossby waves responding to forcing in the North Atlantic.

The Atlantic Multidecadal Oscillation is a mode of climate variability based on the average anomalies of sea surface temperature (SST) in the North Atlantic with a period between 60-80 yrs. Although the instrumental record for AMO is relatively short (~150 years), it provides an example for ocean-atmosphere interaction involving changes in north-to-south circulation and overturning of water and heat in the Atlantic Ocean. According to recent models, AMO variability is associated with changes in Atlantic Meridional Overturning Circulation (AMOC)

circulation (de Beurs et al., 2018; Bothe et al., 2012) a well-documented feature of Heinrich events.

The AMO has a significant influence on regional precipitation in Central Asia (Bothe et al., 2012; Tan and Shao, 2017). The precipitation amount index–which reflects the varying weight of daily precipitation and calculates the contribution of days with the largest precipitation to the annual precipitation (Martin-Vide, 2004)–calculated for AMO and Central Asia showed AMO had a strong influence on the annual scale from 1976–2016 (Yang et al., 2020). Significant decreases in precipitation concentration index were likely related to positive phases of AMO. This indicates negative phases of AMO, characterized by cooler SST over the North Atlantic likely causes increased precipitation over our cave site.

In summary, the three circulation patterns, NOA (+ phase), EA/WR (-phase) and the AMO (-phase) are the most likely atmospheric circulation scenarios which reconcile the signals in our data during H4 and H5. Heinrich events caused a slow down the AMOC, altering the North Atlantic SST in effect, changing atmospheric circulation patters which may have intensified the Westerly Jet or caused an eastward shift of the Siberian High. The AMO serves as an analog for interpreting melt water induced climate changes in the North Atlantic and the atmospheric teleconnections with mid-latitude winter precipitation climates like Central Asia. In conclusion, the hydro-climate is influenced by the interaction of North Atlantic climate change via the connection of larger weather patterns which control the Westerly Jet and Siberian High.

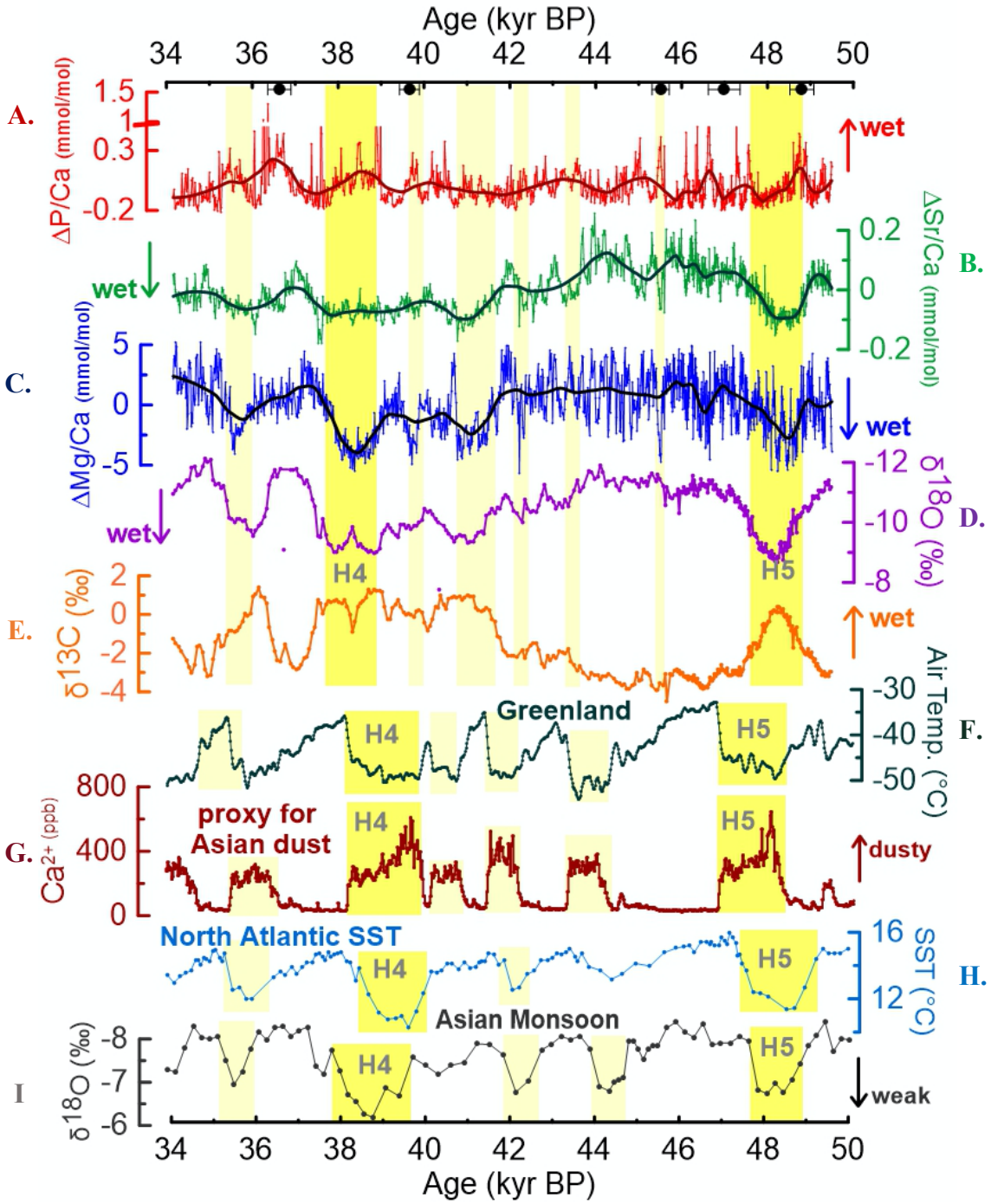

Figure 11. CU1-1 comparison of proxy-based paleoclimate proxy reconstructions:
A) ΔP/Ca, B) ΔSr/Ca, C) ΔMg/Ca normalized to their respective averages (mmol/mol) and D) $\delta^{18}O$ and E) $\delta^{13}C$ (VPDB ‰) taken from a Kyrgyz stalagmite, CU1-1 (this paper) compared with global climate changes presented in various records. Wet climate conditions above the cave are indicated by an increase in ΔP/Ca and a decrease in ΔSr/Ca and ΔMg/Ca and high $\delta^{18}O$ and $\delta^{13}C$ values. Considering individual age model uncertainty (~0.2-0.37 kyr BP), highlighted sections show climate events in response to H4 (38-39 kyr BP) and H5 (47-49 kyr

BP) occurring synchronously with wet climate conditions above CU cave. The H4 and H5 time windows are characterized by F) North Atlantic cooling, G) invigorated dust cycle, H) decreased North Atlantic SST, and a I) weakened Asian Monsoon. Potential patterns of wet climate in Central Asia occurring in concert with climate changes in the northern high latitudes and the tropics, such as those during H4 and H5, are highlighted with lighter hues of yellow. (Air Temperature (ºC) Reconstruction from NRGIP Ice core (± 0.02) taken from Kindler et al., (2014); Dissolved Calcium Ion concentration measured in Greenland Ice core (GISP2) taken from Rasmussen et al., (2006) and Seierstad et al., (2014); North Atlantic SST (ºC) estimation from sediment core MD01-2444 taken from Matrat et al., (2007); Stable Oxygen Isotope data from Hulu Cave, China measures strength of Asian Monsoon, taken from Wang et al., (2001)).

6. Summary and Conclusion

In a stalagmite from Central Asia (southwestern Kyrgyzstan) we analyzed several trace elements and carbon and oxygen isotopes. We focus on Mg/Ca, Sr/Ca, and P/Ca ratios and $\delta^{18}O$ and $\delta^{13}C$ values as proxies for hydroclimate changes. The Sr/Ca and Mg/Ca compositions are positively correlated with each other, indicating that Prior Calcite Precipitation is most likely the dominant factor responsible for partitioning Mg and Sr into calcite. We rule out aluminosilicate contribution as a potential cause for the relationship between Mg/Ca and Sr/Ca. However, temperature and growth rate likely played a role in co-shaping Mg/Ca and Sr/Ca variation, respectively. After identifying PCP as the main driver for trace element incorporation, we used ΔMg/Ca, ΔSr/Ca, and ΔP/Ca as proxies for precipitation reconstruction and identify several intervals of wet phase in Central Asia. A comparison of the trace element results with the stable oxygen and carbon isotope data supports our interpretation of PCP to be the driving mechanisms behind TE/ Ca and stable isotope signatures in CU1-1. $\delta^{18}O$ and $\delta^{13}C$ show a strong, positive and significant correlation with each other and exhibit high values in CU1-1 during wet phases over the cave, and vice versa.

A comparison of our results with prominent records of northern hemisphere high and low latitude climate changes shows that several episodes of precipitation increase in Central Asia coincide with freshwater-induced cooling of North Atlantic and the weakening of the northern hemisphere monsoon system. We conclude that there are strong atmospheric circulation changes linking freshwater-induced climate changes in North Atlantic and hydroclimate changes in Central Asia. Furthermore, we propose two atmospheric links between a North Atlantic and Central Asia to be largely influenced by the strength of the Westerly Jet, and eastward position of the Siberian High which would bring increased moisture to the Central Asia when the North Atlantic cools.

7. References

1. Acker, J. G., & Leptoukh, G. (2007). Online analysis enhances use of NASA earth science data. *Eos, Transactions American Geophysical Union*, *88*(2), 14-17.

2. Badino, G. (2004). Cave temperatures and global climate change. In *International Journal of Speleology*.

3. Barker, S., Chen, J., Gong, X., Jonkers, L., Knorr, G., & Thornalley, D. (2015). Icebergs not the trigger for North Atlantic cold events. *Nature*, *520*(7547), 333-336.

4. Bond, G., Broecker, W., Johnsen, S., McManus, J., Labeyrie, L., Jouzel, J., & Bonani, G. (1993). Correlations between climate records from North Atlantic sediments and Greenland ice. *Nature*, *365*(6442), 143-147.

5. Bjorck, S., Walker, M, J., Cwynar, L. C., Johnsen, S., Knudsen, K. L., Lowe, J. J., & Wohlfarth, B. (1998). An even stratigraphy for the Last Termination in the North Atlantic region based on the Greenland ice-core record: a proposal by the INTIMATE group. *Journal of Quaternary Science: Published for the Quaternary Research Association, 13(4), 283-292*.

6. Blisniuk, P. M., & Stern, L. A. (2005). Stable isotope paleoaltimetry: A critical review. *American Journal of Science*, *305*(10), 1033-1074.

7. de Beurs, K. M., Henebry, G. M., Owsley, B. C., & Sokolik, I. N. (2018). Large scale climate oscillation impacts on temperature, precipitation and land surface phenology in Central Asia. *Environmental Research Letters*, *13*(6), 065018.

8. Bothe, O., Fraedrich, K., & Zhu, X. (2012). Precipitation climate of Central Asia and the large-scale atmospheric circulation. *Theoretical and applied climatology*, *108*(3), 345-354.

9. Breecker, D. O. (2017). Atmospheric pCO2 control on speleothem stable carbon isotope compositions. *Earth and Planetary Science Letters*, *458*, 58-68.

10. Burns, S. J., Godfrey, L. R., Faina, P., McGee, D., Hardt, B., Ranivoharimanana, L., & Randrianasy, J. (2016). Rapid human-induced landscape transformation in Madagascar at the end of the first millennium of the Common Era. *Quaternary Science Reviews*, 134, 92–99.

11. Caesar, L., Rahmstorf, S., Robinson, A., Feulner, G., & Saba, V. (2018). Observed fingerprint of a weakening Atlantic Ocean overturning circulation. *Nature*, *556*(7700), 191-196.

12. Cruz Jr, F. W., Karmann, I., Viana Jr, O., Burns, S. J., Ferrari, J. A., Vuille, M., ... & Moreira, M. Z. (2005). Stable isotope study of cave percolation waters in subtropical

Brazil: Implications for paleoclimate inferences from speleothems. *Chemical Geology*, *220*(3-4), 245-262.

13. Day, C. C., & Henderson, G. M. (2011). Oxygen isotopes in calcite grown under cave-analogue conditions. *Geochimica et Cosmochimica Acta*, *75*(14), 3956-3972.

14. Day, C. C., & Henderson, G. M. (2013). Controls on trace-element partitioning in cave-analogue calcite. *Geochimica et Cosmochimica Acta*, *120*, 612-627.

15. Deplazes, G., Lückge, A., Peterson, L. C., Timmermann, A., Hamann, Y., Hughen, K. A., ... & Haug, G. H. (2013). Links between tropical rainfall and North Atlantic climate during the last glacial period. *Nature Geoscience*, *6*(3), 213-217.

16. Ding, Y., & Krishnamurti, T. N. (1987). Heat budget of the Siberian high and the winter monsoon. *Monthly Weather Review*, *115*(10), 2428-2449.

17. Edwards, R. L., Chen, J. H., & Wasserburg, G. J. (1987). ^{238}U–^{234}U–^{230}Th–^{232}Th systematics and the precise measurement of time over the past 500,000 years. *Earth and Planetary Science Letters*, 81(2–3), 175–192.

18. Eggins, S. M., Kinsley, L. P. J., & Shelley, J. M. G. (1998). Deposition and element fractionation processes during atmospheric pressure laser sampling for analysis by ICP-MS. *Applied Surface Science*, *127*, 278-286.

19. Eggins, S. M., Grün, R., McCulloch, M. T., Pike, A. W., Chappell, J., Kinsley, L., ... & Taylor, L. (2005). In situ U-series dating by laser-ablation multi-collector ICPMS: new prospects for Quaternary geochronology. *Quaternary Science Reviews*, *24*(23-24), 2523-2538.

20. Edwards, R. L., Chen, J. H., & Wasserburg, G. J. (1987). ^{238}U–^{234}U–^{230}Th–^{232}Th systematics and the precise measurement of time over the past 500,000 years. *Earth and Planetary Science Letters*, **81**(2–3), 175– 192.

21. Fairchild, I. J., Borsato, A., Tooth, A. F., Frisia, S., Hawkesworth, C. J., Huang, Y., ... & Spiro, B. (2000). Controls on trace element (Sr–Mg) compositions of carbonate cave waters: implications for speleothem climatic records. *Chemical geology*, *166*(3-4), 255-269.

22. Fairchild, I. J., & Treble, P. C. (2009). Trace elements in speleothems as recorders of environmental change. *Quaternary Science Reviews*, *28*(5-6), 449-468.

23. Gastineau, G., & Frankignoul, C. (2015). Influence of the North Atlantic SST variability on the atmospheric circulation during the twentieth century. *Journal of Climate*, *28*(4), 1396-1416.

24. Gastineau, G., D'Andrea, F., & Frankignoul, C. (2013). Atmospheric response to the North Atlantic Ocean variability on seasonal to decadal time scales. *Climate dynamics*, *40*(9), 2311-2330.

25. Gascoyne, M. (1992). Palaeoclimate determination from cave calcite deposits. *Quaternary Science Reviews*, *11*(6), 609-632.

26. Garbe-Schönberg, D., & Müller, S. (2014). Nano-particulate pressed powder tablets for LA-ICP-MS. *Journal of Analytical Atomic Spectrometry*, *29*(6), 990-1000.

27. Gerlitz, L., Steirou, E., Schneider, C., Moron, V., Vorogushyn, S., & Merz, B. (2018). Variability of the cold season climate in Central Asia. Part I: weather types and their tropical and extratropical drivers. *Journal of climate*, *31*(18), 7185-7207.

28. Gong, D. Y., & Ho, C. H. (2002). The Siberian High and climate change over middle to high latitude Asia. *Theoretical and applied climatology*, *72*(1), 1-9.

29. Gong, D. Y., Wang, S. W., & Zhu, J. H. (2001). East Asian winter monsoon and Arctic oscillation. *Geophysical Research Letters*, *28*(10), 2073-2076.

30. Grinsted, A., Moore, J. C., & Jevrejeva, S. (2004). Application of the cross wavelet transform and wavelet coherence to geophysical time series. *Nonlinear processes in geophysics*, *11*(5/6), 561-566.

31. Hijioka, Y., E. Lin, J.J. Pereira, R.T. Corlett, X. Cui, G.E. Insarov, R.D. Lasco, E. Lindgren, and A. Surjan, (2014): Asia. In: *Climate Change (2014): Impacts, Adaptation, and Vulnerability.* Part B: Regional Aspects. Contribution of Working Group II to the Fifth Assessment Report of the Intergovernmental Panel on Climate Change [Barros, V.R., C.B. Field, D.J. Dokken, M.D. Mastrandrea, K.J. Mach, T.E. Bilir, M. Chatterjee, K.L. Ebi, Y.O. Estrada, R.C. Genova, B. Girma, E.S. Kissel, A.N. Levy, S. MacCracken, P.R. Mastrandrea, and L.L.White (eds.)]. Cambridge University Press, Cambridge, United Kingdom and New York, NY, USA, pp. 1327-1370.

32. Heinrich, H. (1988). Origin and consequences of cyclic ice rafting in the northeast Atlantic Ocean during the past 130,000 years. *Quaternary research*, *29*(2), 142-152.

33. Hemming, S. R. (2004). Heinrich events: Massive late Pleistocene detritus layers of the North Atlantic and their global climate imprint. *Reviews of Geophysics*, *42*(1).

34. Hilmer, M., & Jung, T. (2000). Evidence for a recent change in the link between the North Atlantic Oscillation and Arctic Sea ice export. *Geophysical Research Letters*, *27*(7), 989-992.

35. Hren, M. T., Bookhagen, B., Blisniuk, P. M., Booth, A. L., & Chamberlain, C. P. (2009). Δ and Tibetan Plateau: Implications for moisture sources and paleoelevation reconstructions.20 32. https://doi.org/10.1016/j.epsl.2009.08.041

36. Huang, Y., Fairchild, I. J., Borsato, A., Frisia, S., Cassidy, N. J., McDermott, F., & Hawkesworth, C. J. (2001). Seasonal variations in Sr, Mg and P in modern speleothems (Grotta di Ernesto, Italy). *Chemical Geology*, *175*(3-4), 429-448.

37. Kylander-Clark, A. R., Hacker, B. R., & Cottle, J. M. (2013). Laser-ablation split-stream ICP petrochronology. *Chemical Geology*, *345*, 99-112.

38. Krichak, S. O., & Alpert, P. (2005). Decadal trends in the east Atlantic–west Russia pattern and Mediterranean precipitation. *International journal of climatology: a journal of the Royal Meteorological Society*, *25*(2), 183-192.

39. Knutti, R., Flückiger, J., Stocker, T. F., & Timmermann, A. (2004). Strong hemispheric coupling of glacial climate through freshwater discharge and ocean circulation. *Nature*, *430*(7002), 851-856.

40. Kindler, P., Guillevic, M., Baumgartner, M., Schwander, J., Landais, A., & Leuenberger, M. (2014). Temperature reconstruction from 10 to 120 kyr b2k from the NGRIP ice core. *Climate of the Past*, *10*(2), 887-902.

41. Lenton, T. M., Held, H., Kriegler, E., Hall, J. W., Lucht, W., Rahmstorf, S., & Schellnhuber, H. J. (2008). Tipping elements in the Earth's climate system. *Proceedings of the national Academy of Sciences*, *105*(6), 1786-1793.

42. Lide, D. R., & Kehiaian, H. V. (2020). *CRC handbook of thermophysical and thermochemical data*. Crc Press.

43. Lachniet, M. S. (2009). Climatic and environmental controls on speleothem oxygen-isotope values. Quaternary Science Reviews, 28(5-6), 412-432.

44. Lead, J. R., & Wilkinson, K. J. (2006). Aquatic colloids and nanoparticles: current knowledge and future trends. *Environmental Chemistry*, *3*(3), 159-171.

45. Lim, Y. K. (2015). The East Atlantic/West Russia (EA/WR) teleconnection in the North Atlantic: climate impact and relation to Rossby wave propagation. *Climate dynamics*, *44*(11), 3211-3222.

46. Ma, Y., Weldeab, S., Schneider, R. R., Andersen, N., Garbe-Schönberg, D., & Friedrich, T. (2021). Strong Southern African Monsoon and weak Mozambique Channel throughflow during Heinrich events: Implication for Agulhas leakage. *Earth and Planetary Science Letters*, *574*, 117148.

47. MacAyeal, D. R. (1993). Binge/purge oscillations of the Laurentide ice sheet as a cause of the North Atlantic's Heinrich events. *Paleoceanography*, *8*(6), 775-784.

48. Martrat, B., Grimalt, J. O., Shackleton, N. J., de Abreu, L., Hutterli, M. A., & Stocker, T. F. (2007). Four climate cycles of recurring deep and surface water destabilizations on the Iberian margin. *Science*, *317*(5837), 502-507.

49. Marks, S. G., Medina-Elizalde, M., Burns, S., Weldeab, S., Lases-Hernandez, F., Cazares, G., & McGee, D. (2021). Evidence for Decreased Precipitation Variability in the Yucatán Peninsula During the Mid-Holocene. *Paleoceanography and Paleoclimatology*, *36*(5), e2021PA004219.

50. Martin-Vide, J. (2004). Spatial distribution of a daily precipitation concentration index in peninsular Spain. *International Journal of Climatology: A Journal of the Royal Meteorological Society*, *24*(8), 959-971.

51. Mucci, A., & Morse, J. W. (1983). The incorporation of Mg2+ and Sr2+ into calcite overgrowths: influences of growth rate and solution composition. *Geochimica et Cosmochimica Acta*, *47*(2), 217-233.

52. Novello, V. F., Cruz, F. W., Vuille, M., Stríkis, N. M., Edwards, R. L., Cheng, H., ... & Santos, R. V. (2017). A high-resolution history of the South American Monsoon from Last Glacial Maximum to the Holocene. *Scientific reports*, *7*(1), 1-8.

53. Nakamura, T., Yamazaki, K., Iwamoto, K., Honda, M., Miyoshi, Y., Ogawa, Y., & Ukita, J. (2015). A negative phase shift of the winter AO/NAO due to the recent Arctic sea-ice reduction in late autumn. *Journal of Geophysical Research: Atmospheres*, *120*(8), 3209-3227.

54. Paton, C., Woodhead, J. D., Hellstrom, J. C., Hergt, J. M., Greig, A., & Maas, R. (2010). Improved laser ablation U-Pb zircon geochronology through robust downhole fractionation correction. *Geochemistry, Geophysics, Geosystems*, *11*(3).

55. Pausata, F. S. R., Battisti, D. S., Nisancioglu, K. H., & Bitz, C. M. (2011). Chinese stalagmite δ18O controlled by changes in the Indian monsoon during a simulated Heinrich event. Nature Geoscience, 4(7), 474 480. https://doi.org/10.1038/ngeo1169

56. Rahmstorf, S. (2002). Ocean circulation and climate during the past 120,000 years. *Nature*, *419*(6903), 207-214.

57. Rahmstorf, S. (2006). Thermohaline ocean circulation. *Encyclopedia of quaternary sciences*, *5*.

58. Rasmussen, S. O., Andersen, K. K., Svensson, A. M., Steffensen, J. P., Vinther, B. M., Clausen, H. B., ... & Ruth, U. (2006). A new Greenland ice core chronology for the last glacial termination. *Journal of Geophysical Research: Atmospheres*, *111*(D6).

59. Rimstidt, J. D., Balog, A., & Webb, J. (1998). Distribution of trace elements between carbonate minerals and aqueous solutions. *Geochimica et Cosmochimica Acta*, 62(11), 1851-1863.

60. Rudnick, R. L., Gao, S., Holland, H. D., & Turekian, K. K. (2003). Composition of the continental crust. *The crust*, *3*, 1-64.

61. Schiemann, R., Lüthi, D., Vidale, P. L., & Schär, C. (2008). The precipitation climate of Central Asia—intercomparison of observational and numerical data sources in a remote semiarid region. International Journal of Climatology: A Journal of the Royal Meteorological Society, 28(3), 295-314.

62. Seierstad, I. K., Abbott, P. M., Bigler, M., Blunier, T., Bourne, A. J., Brook, E., ... & Vinther, B. M. (2014). Consistently dated records from the Greenland GRIP, GISP2 and NGRIP ice cores for the past 104 ka reveal regional millennial-scale δ18O gradients with possible Heinrich event imprint. *Quaternary Science Reviews*, *106*, 29-46.

63. Sinclair, D. J., Banner, J. L., Taylor, F. W., Partin, J., Jenson, J., Mylroie, J., ... & Miklavič, B. (2012). Magnesium and strontium systematics in tropical speleothems from the Western Pacific. *Chemical Geology*, *294*, 1-17.

64. Scholz, D., & Hoffmann, D. L. (2011). StalAge–An algorithm designed for construction of speleothem age models. *Quaternary Geochronology*, *6*(3-4), 369-382.

65. Stríkis, N. M., Cruz, F. W., Barreto, E. A., Naughton, F., Vuille, M., Cheng, H., ... & Sales, H. R. (2018). South American monsoon response to iceberg discharge in the North Atlantic. *Proceedings of the National Academy of Sciences*, *115*(15), 3788-3793.

66. Swann, G. E., Mackay, A. W., Leng, M. J., & Demory, F. (2005). Climatic change in Central Asia during MIS 3/2: a case study using biological responses from Lake Baikal. *Global and Planetary Change*, *46*(1-4), 235-253.

67. Syed, F. S., Giorgi, F., Pal, J. S., & Keay, K. (2010). Regional climate model simulation of winter climate over Central–Southwest Asia, with emphasis on NAO and ENSO effects. *International Journal of Climatology: A Journal of the Royal Meteorological Society*, *30*(2), 220-235.

68. Tan, X., & Shao, D. (2017). Precipitation trends and teleconnections identified using quantile regressions over Xinjiang, China. *International Journal of Climatology*, *37*(3), 1510-1525.

69. Taylor, S. R., & McLennan, S. M. (1985). The continental crust: Its composition and evolution. An examination of the geochemical record preserved in sedimentary rocks. Blackwell Scientific.

70. Tesoriero, A. J., & Pankow, J. F. (1996). Solid solution partitioning of Sr2+, Ba2+, and Cd2+ to calcite. *Geochimica et Cosmochimica Acta*, *60*(6), 1053-1063.

71. Tooth, A. F., & Fairchild, I. J. (2003). Soil and karst aquifer hydrological controls on the geochemical evolution of speleothem-forming drip waters, Crag Cave, southwest Ireland. *Journal of Hydrology*, *273*(1-4), 51-68.

72. Tropical Rainfall Measuring Mission (TRMM) (2011), TRMM (TMPA/3B43) Rainfall Estimate L3 1 month 0.25 degree x 0.25 degree V7, Greenbelt, MD, Goddard Earth Sciences Data and Information Services Center (GES DISC), Accessed: [2021], 10.5067/TRMM/TMPA/MONTH/7

73. Wang, Y. J., Cheng, H., Edwards, R. L., An, Z. S., Wu, J. Y., Shen, C. C., & Dorale, J. A. (2001). A high-resolution absolute-dated late Pleistocene monsoon record from Hulu Cave, China. *Science*, *294*(5550), 2345-2348.

74. Wang, Y. J., Cheng, H., Edwards, R. L., An, Z. S., Wu, J. Y., Shen, C. C., & Dorale, J. A. (2001). A high-resolution absolute-dated late Pleistocene monsoon record from Hulu Cave, China. *Science*, *294*(5550), 2345-2348.

75. Wang, C. (2019). Three-ocean interactions and climate variability: a review and perspective. *Climate Dynamics*, *53*(7), 5119-5136.

76. Wan, Z., Hook, S., Hulley, G. (2015). *MOD11C3 MODIS/Terra Land Surface Temperature/Emissivity Monthly L3 Global 0.05Deg CMG V006* [Data set]. NASA EOSDIS Land Processes DAAC. Accessed 2022-06-11 from https://doi.org/10.5067/MODIS/MOD11C3.006

77. Weldeab, S., Lea, D. W., Schneider, R. R., & Andersen, N. (2007). 155,000 years of West African monsoon and ocean thermal evolution. *science*, *316*(5829), 1303-1307.

78. Woodhead, J. D., Hellstrom, J., Hergt, J. M., Greig, A., & Maas, R. (2007). Isotopic and elemental imaging of geological materials by laser ablation inductively coupled plasma-mass spectrometry. *Geostandards and Geoanalytical Research*, *31*(4), 331-343.

79. Yao, T., Masson Delmotte, V., Gao, J., Yu, W., Yang, X., Risi, C., et al. (2013). A review of climatic controls on δ Tibetan Plateau: Observations and simulations. Reviews of Geophysics, 51, 525 548.

80. Yang, T., Li, Q., Chen, X., De Maeyer, P., Yan, X., Liu, Y., ... & Li, L. (2020). Spatiotemporal variability of the precipitation concentration and diversity in Central Asia. *Atmospheric Research*, *241*, 104954.